

Kepler Observations of the Asteroseismic Binary HD 176465

T. R. White^{1,2,3}, O. Benomar^{4,5}, V. Silva Aguirre¹, W. H. Ball^{2,3}, T. R. Bedding^{6,1}, W. J. Chaplin^{7,1}, J. Christensen-Dalsgaard¹, R. A. Garcia⁸, L. Gizon^{3,2,5}, D. Stello^{6,1}, S. Aigrain⁹, H. M. Antia¹⁰, T. Appourchaux¹¹, M. Bazot⁵, T. L. Campante^{7,1}, O. L. Creevey¹², G. R. Davies^{7,1,8}, Y. P. Elsworth^{7,1}, P. Gaulme^{13,14}, R. Handberg¹, S. Hekker^{3,1}, G. Houdek¹, R. Howe⁷, D. Huber^{6,15,1}, C. Karoff^{1,16}, J. P. Marques¹⁷, S. Mathur¹⁸, A. McQuillan¹⁹, T. S. Metcalfe¹⁸, B. Mosser²⁰, M. B. Nielsen^{2,3}, C. Régulo^{21,22}, D. Salabert⁸, and T. Stahn^{2,3}

¹ Stellar Astrophysics Centre, Department of Physics and Astronomy, Aarhus University, Ny Munkegade 120, DK-8000 Aarhus C, Denmark; e-mail: tim@phys.au.dk

² Institut für Astrophysik, Georg-August-Universität Göttingen, Friedrich-Hund-Platz 1, 37077 Göttingen, Germany

³ Max-Planck-Institut für Sonnensystemforschung, Justus-von-Liebig-Weg 3, 37077 Göttingen, Germany

⁴ Department of Astronomy, The University of Tokyo, School of Science, Tokyo 113-0033, Japan

⁵ Center for Space Science, NYUAD Institute, New York University Abu Dhabi, PO Box 129188, Abu Dhabi, UAE

⁶ Sydney Institute for Astronomy (SIfA), School of Physics, University of Sydney, NSW 2006, Australia

⁷ School of Physics and Astronomy, University of Birmingham, Birmingham B15 2TT, UK

⁸ Laboratoire AIM, CEA/DRF – CNRS – Univ. Paris Diderot – IRFU/SAP, Centre de Saclay, 91191 Gif-sur-Yvette Cedex, France

⁹ Oxford Astrophysics, University of Oxford, Keble Rd, Oxford OX1 3RH, UK

¹⁰ Tata Institute of Fundamental Research, Homi Bhabha Road, Mumbai 400005, India

¹¹ Univ. Paris-Sud, Institut d'Astrophysique Spatiale, UMR 8617, CNRS, Bâtiment 121, 91405 Orsay Cedex, France

¹² Laboratoire Lagrange, Université Côte d'Azur, Observatoire de la Côte d'Azur, CNRS, Blvd de l'Observatoire, CS 34229, 06304 Nice cedex 4, France

¹³ Department of Astronomy, New Mexico State University, P.O. Box 30001, MSC 4500, Las Cruces, NM 88003-8001, USA

¹⁴ Apache Point Observatory, 2001 Apache Point Road, P.O. Box 59, Sunspot, NM 88349, USA

¹⁵ SETI Institute, 189 Bernardo Avenue, Suite 100, Mountain View, CA 94043, USA

¹⁶ Department of Geoscience, Aarhus University, Høegh-Guldbergs Gade 2, 8000, Aarhus C, Denmark

¹⁷ LESIA, CNRS, Université Pierre et Marie Curie, Université Denis Diderot, Observatoire de Paris, 92195 Meudon Cedex, France

¹⁸ Space Science Institute, 4750 Walnut St. Suite 205, Boulder CO 80301, USA

¹⁹ School of Physics and Astronomy, Raymond and Beverly Sackler, Faculty of Exact Sciences, Tel Aviv University, 69978, Tel Aviv, Israel

²⁰ LESIA, Observatoire de Paris, PSL Research University, CNRS, Sorbonne Universités, UPMC Univ. Paris 06, Univ. Paris Diderot, Sorbonne Paris Cité

²¹ Instituto de Astrofísica de Canarias, 38205 La Laguna, Tenerife, Spain

²² Universidad de La Laguna, Dpto. de Astrofísica, 38206 La Laguna, Tenerife, Spain

Received Month Day, Year; accepted Month Day, Year

ABSTRACT

Binary star systems are important for understanding stellar structure and evolution, and are especially useful when oscillations can be detected and analysed with asteroseismology. However, only four systems are known in which solar-like oscillations are detected in both components. Here, we analyse the fifth such system, HD 176465, which was observed by *Kepler*. We carefully analysed the system's power spectrum to measure individual mode frequencies, adapting our methods where necessary to accommodate the fact that both stars oscillate in a similar frequency range. We also modelled the two stars independently by fitting stellar models to the frequencies and complementary parameters. We are able to cleanly separate the oscillation modes in both systems. The stellar models produce compatible ages and initial compositions for the stars, as is expected from their common and contemporaneous origin. Combining the individual ages, the system is about 3.0 ± 0.5 Gyr old. The two components of HD 176465 are young physically-similar oscillating solar analogues, the first such system to be found, and provide important constraints for stellar evolution and asteroseismology.

Key words. asteroseismology – methods: data analysis – stars: individual: HD 176465

1. Introduction

Observations of binary stars have been critical in advancing our knowledge of stellar structure and evolution. The shared formation history of stars in these systems results in their having the same initial chemical composition and age. Additionally, the dynamics of the system can reveal the component masses, and their radii if they eclipse.

Studies of binary stars can be further enhanced by asteroseismic measurements. Asteroseismology of solar-like stars is rapidly proving its effectiveness at characterising stars, driven by the successes of the CoRoT and *Kepler* space telescopes (Michel et al. 2008; Gilliland et al. 2010a; Chaplin et al. 2011). However, few binary systems have solar-like oscillations detected in both components.

Three systems exist in which the two components have been observed separately: α Cen A (e.g. Bouchy & Carrier 2002; Bedding et al. 2004; Fletcher et al. 2006; Bazot et al. 2007), and B (Carrier & Bourban 2003; Kjeldsen et al. 2005), 16 Cyg A and B (KIC 12069424 and KIC 12069449; Metcalfe et al. 2012, 2015; Davies et al. 2015), and HD 176071 (KIC 9139151 and KIC 9139163; Appourchaux et al. 2012). Additionally, oscillations in both components of HD 177412 (HIP 93511) have been measured while observed as a single *Kepler* target, KIC 7510397 (Appourchaux et al. 2015).

More commonly, oscillations have been detected in one member of a binary system (e.g. Mathur et al. 2013), particularly amongst the many red giants that have been observed (e.g. Hekker et al. 2010b; Frandsen et al. 2013; Gaulme et al. 2013, 2014; Beck et al. 2014; Rawls et al. 2016). In addition, KIC 4471379 (Murphy et al. 2014) is a binary in which both components are δ Scuti pulsators, while KIC 10080943 (Schmid et al. 2015; Keen et al. 2015) has two γ Doradus/ δ Scuti hybrids.

Kepler has detected oscillations in hundreds of Sun-like stars (Chaplin et al. 2011, 2014). With an estimated 60% of stars thought to be multiple systems, it might be expected that *Kepler* will have observed many unresolved binary systems, some of which should exhibit oscillations in both components. However, Miglio et al. (2014) used population synthesis models to predict that such systems are rare due to the requirement that both stars have oscillations with similar amplitudes in order to be detected. For this, they must have similar luminosity-to-mass ratios (Kjeldsen & Bedding 1995). Despite this, HD 177412 contains unequal components. The primary star of this system is ~ 2.25 times more luminous than the secondary, and the ranges in which their oscillation modes are excited are well-separated in frequency (Appourchaux et al. 2015). In this case, the system was sufficiently bright ($V = 7.9$ mag) that the oscillation modes of the secondary star could still be detected.

In this paper we report on another asteroseismic binary showing solar-like oscillations in both components. It corresponds to the previously-known binary HD 176465, which has been observed as a single *Kepler* target, KIC 10124866¹. HD 176465 was identified as a visual binary from 1902 observations as part of the Astrogaphic Catalogue (Urban et al. 1998), and has since been observed on multiple occasions (Mason et al. 2001). With a Tycho visual magnitude of 8.537, the primary, HD 176465 A is only ~ 1.2 times more luminous than HD 176465 B ($V_T = 8.674$ mag), in line with the expectations of Miglio et al. (2014). Due to the similarity of the stars, their oscillation modes are excited at similar frequencies, complicating their analysis. In this paper we present the determination of the oscillation mode parameters and detailed asteroseismic models of both HD 176465 A and B.

2. Observations

HD 176465 was observed by the *Kepler* space telescope in short-cadence mode (SC; 58.85 s sampling) for 30 days during the asteroseismic survey phase (20 Jul 2009 to 19 Aug 2009, Q2.2), and continuously after the end of the survey (37 months, Q5–Q17). Additionally, the system was observed in the long-cadence mode (LC; 29.43 min sampling) for the entire nominal mission (4 years, Q0–Q17), although this sampling is not rapid enough to sample frequencies of the solar-like oscillations, which are well

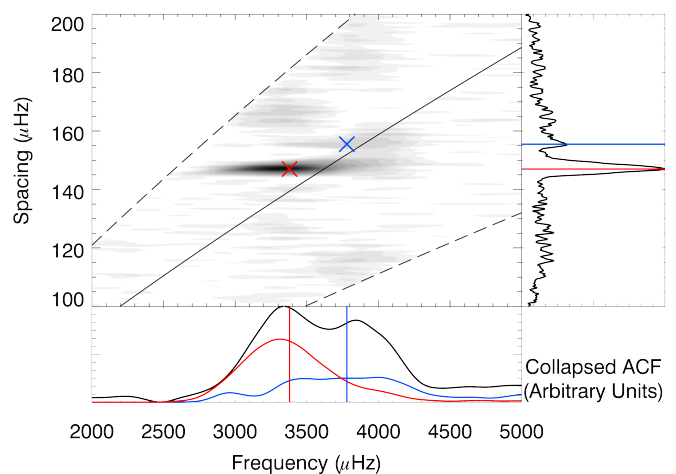


Fig. 2. Localized autocorrelation of the power spectrum of HD 176465. Two peaks in the autocorrelation function are visible, corresponding to the primary and secondary components of HD 176465 (red and blue crosses, respectively). The solid line shows the mean observed relation between $\Delta\nu$ and ν_{\max} (Stello et al. 2009), while the dashed lines are 0.7 and 1.3 times this value. The collapsed autocorrelation function (ACF) along each axis are shown in black in the lower and right panels, with the peaks indicated by red and blue lines. The red and blue curves in the lower panel show the collapsed ACF with spacings around 147 and 155 μHz , respectively.

above the LC Nyquist frequency. The SC time series were prepared from the raw observations as described by Jenkins et al. (2010) and further corrected to remove outliers and jumps as described by García et al. (2011). Figure 1 shows the smoothed power spectrum of the short-cadence time series.

The signature of solar-like oscillations is a broad, Gaussian-like hump of power comprised of approximately equally-spaced modes. The frequency of maximum oscillation power is denoted ν_{\max} , and the oscillation frequencies are well approximated by the asymptotic relation (Vandakurov 1967; Tassoul 1980; Gough 1986)

$$\nu_{n,l} \approx \Delta\nu \left(n + \frac{l}{2} + \epsilon \right) - \delta\nu_{0l}, \quad (1)$$

where $\Delta\nu$, called the large separation, is the spacing between modes of the same spherical degree l and consecutive radial orders n , $\delta\nu_{0l}$ is the small separation between modes of different degree, and ϵ is a dimensionless phase offset. The presence of solar-like oscillations in both stars is clear in Fig. 1.

Oscillations were detected in the survey data (Q2.2), and the global oscillation parameters $\Delta\nu$ and ν_{\max} were extracted using several automated pipelines (Campante et al. 2010; Christensen-Dalsgaard et al. 2008; Hekker et al. 2010a; Huber et al. 2009; Karoff et al. 2010; Mathur et al. 2010; Mosser & Appourchaux 2009; Roxburgh 2009). Inspection of the autocorrelation function of the power spectrum, shown in Fig. 2, reveals a strong peak that corresponds to the higher-amplitude oscillations of HD 176475 A. While most pipelines were able to make this detection, as they were programmed to seek oscillations from a single star, the presence of a second set of oscillations in the time series was missed.

The realization that the oscillations of this second star were present in the *Kepler* timeseries was made by a manual inspection of the échelle diagram. Figure 3 (left) shows the power spectrum in échelle format with a large separation corresponding to that of the primary, $\Delta\nu = 146.8 \mu\text{Hz}$.

¹ Within the *Kepler* Asteroseismic Science Consortium (KASC), stars have attracted nicknames that have been used by those analysing them. HD 176465 A and B are referred to as “Luke” and “Leia”, respectively.

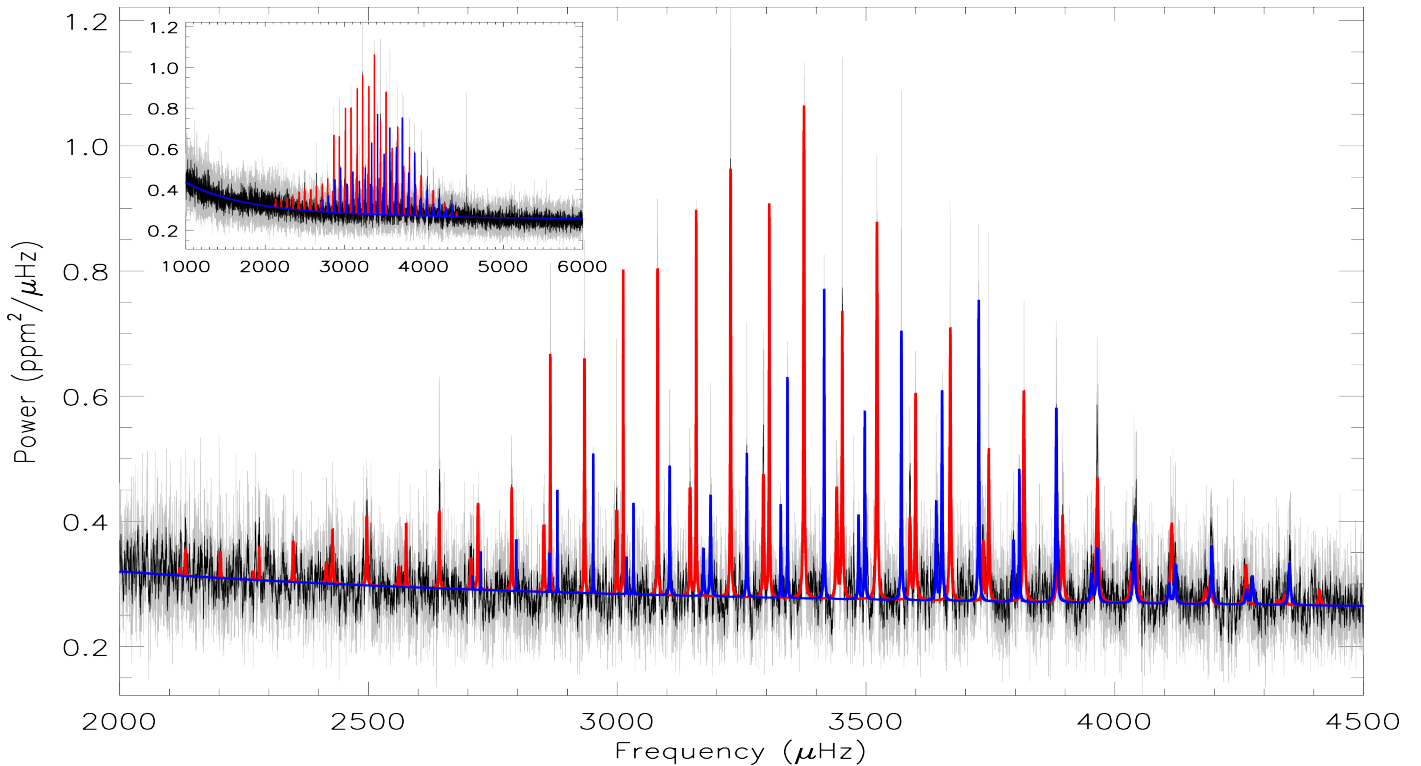


Fig. 1. Power spectrum of HD 176465, smoothed by a box-car filter over $0.5\mu\text{Hz}$ (grey) and $2\mu\text{Hz}$ (black). Superimposed is the best fit of HD 176465A (red) and HD 176465B (blue). The inset shows the power spectrum over a wider range. The peak at $4531\mu\text{Hz}$ is an artifact (see Fig. 3).

Near-vertical ridges in the échelle diagram (red symbols) correspond to modes of various radial orders, n , and the same spherical degree, l . The closely spaced $l = 2, 0$ ridges and the $l = 1$ ridges are clearly visible, from left to right. We also see other modes that do not fall along vertical ridges in this échelle diagram, but instead form sloping ridges (blue symbols).

A diagonal ridge in an échelle diagram means that the large separation is incorrect for those modes. In this case, the value of $\Delta\nu$ is too small but for a larger value, these ridges will become near-vertical. Figure 3 (right) shows the échelle diagram with $\Delta\nu = 155.4\mu\text{Hz}$. The ridges that were diagonal in Fig. 3 (left) have now become vertical, and the formerly vertical ridges are now diagonal, but sloping downwards.

Since the large separation approximately scales with the square root of the mean stellar density (Ulrich 1986), the existence of two distinct values of $\Delta\nu$ indicate the presence of two distinct stars. We can be confident that the oscillations with $\Delta\nu = 146.8\mu\text{Hz}$ are those of HD 176465 A, and oscillations with $\Delta\nu = 155.4\mu\text{Hz}$ are those of HD 176465 B because, for a given age, more massive stars have a lower mean density (Christensen-Dalsgaard 1984).

3. Methods to measure the mode parameters

Extracting accurate mode parameters is an important step required before modelling a star. The most common method is the Maximum Likelihood Estimator (MLE) approach (Anderson et al. 1990), which has been extensively used to analyse the low-degree global acoustic oscillations of the Sun (e.g. Chaplin et al. 1996). For solar-like oscillations, the noise statistics for the power spectral density y_i at a given frequency ν_i is a χ^2 with two

degrees of freedom so that the likelihood is

$$L = \prod_{i=1}^N \frac{1}{M(\nu_i, \theta)} e^{-y_i/M(\nu_i, \theta)}. \quad (2)$$

Here, $M(\nu_i, \theta)$ is the model used to describe the data set $\{\nu_i, y_i\}$ and θ are the parameters of that model. The model of the power spectrum has two components. Firstly, the noise background is comprised of a sum of quasi-Lorentzian functions whose parametrization may vary (Harvey 1985; Karoff 2012) plus a flat white noise level. Secondly, the acoustic p modes are described as a series of Lorentzian profiles, with frequencies, heights, and linewidths to be determined.

The MLE approach is well-suited to cases where the likelihood function has a well-defined single maximum, so that convergence towards an unbiased measure of the fitted parameters is ensured (Appourchaux et al. 1998). In the case of the Sun, this is often the case, mostly because of the very high signal-to-noise of the pulsation modes. However, stellar pulsations often have much lower signal-to-noise ratios, so that the likelihood may have several local maxima. In such a case, MLE methods may not converge towards the true absolute maximum of probability.

A Bayesian approach was proposed to tackle this problem (Benomar et al. 2009a,b; Handberg & Campante 2011; Corsaro & De Ridder 2014). The Bayesian approach uses conditional probabilities and involves Bayes' theorem to define a so-called posterior distribution $\pi(\theta, \mathbf{y}|M)$. This statistical criterion incorporates not only the likelihood $L \equiv \pi(\mathbf{y}|\theta, M)$, but also the *a priori* information $\pi(\theta|M)$ on the fitted parameters,

$$\pi(\theta, \mathbf{y}|M) = \frac{\pi(\theta|M)\pi(\mathbf{y}|\theta, M)}{\pi(\mathbf{y}|M)}. \quad (3)$$

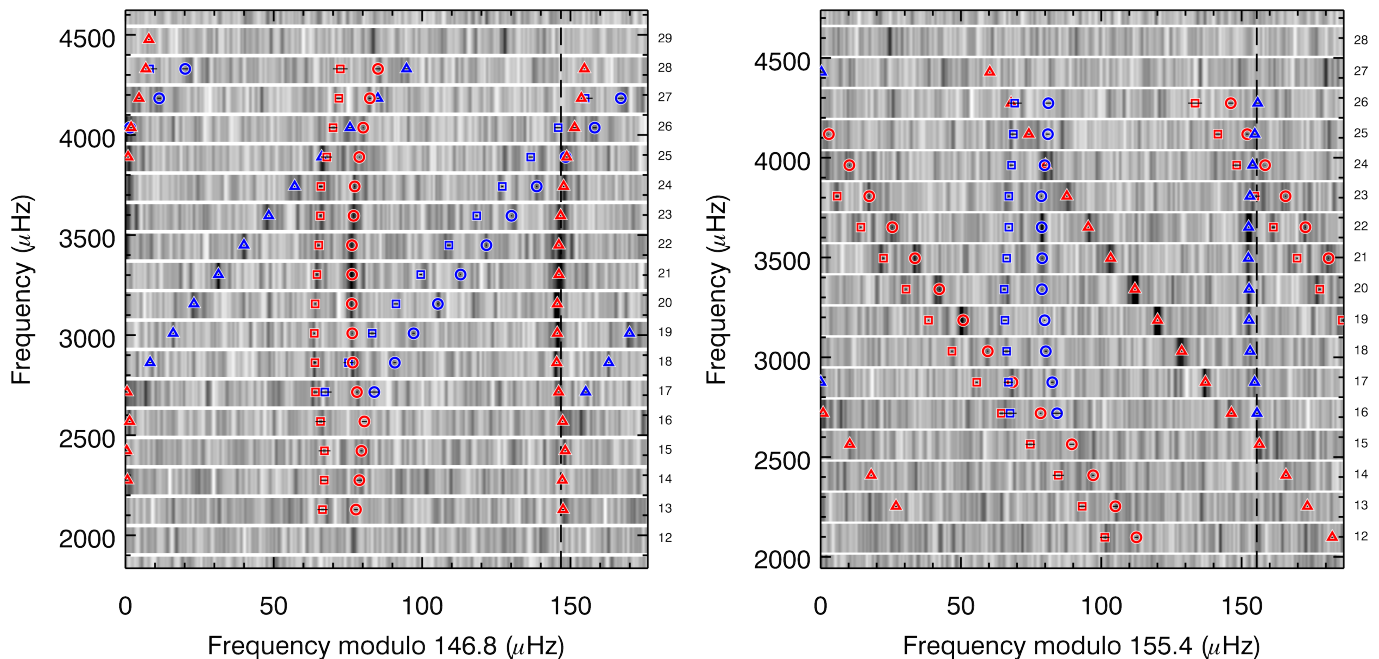


Fig. 3. Échelle diagrams of HD 176465 A (left) and B (right) showing the overlapping sets of modes with different large separations. The fitted frequencies are indicated by the red and blue symbols for the A and B components respectively. Symbol shapes indicate the mode identification: circles are $l = 0$ modes, triangles are $l = 1$ modes, and squares are $l = 2$ modes. For reference, a greyscale map of the smoothed power spectrum is shown in the background. Numbers to the right of the plot indicate radial order of the $l = 0$ modes. To make the location of modes near the edge of the échelle diagrams clearer, the diagrams have been extended in width beyond the value of the large separation, which is indicated by the dashed vertical lines. The peak at 4531 μHz is the 8th harmonic of the *Kepler* long-cadence sampling rate, which is a known artifact (Gilliland et al. 2010b).

Here, $\pi(\mathbf{y}|M)$ corresponds to the global likelihood, linked to the posterior probability of the model given the data,

$$P(M|\mathbf{y}) = \frac{\pi(\mathbf{y}|M)\pi(M)}{\pi(\mathbf{y})}, \quad (4)$$

which is the probability that a model M is consistent with observations \mathbf{y} . This is an essential quantity for comparing competing models, since it defines the level of *evidence* supporting each one of the models. In its most sophisticated and useful form, the Bayesian method uses a sampling algorithm, such as the Markov Chain Monte Carlo (MCMC) sampler. This is actually crucial to calculating the global likelihood². By exploring the full extent of the posterior distribution (within the bounds defined by the priors), one can determine the full probability distribution of each of the parameters. Although it is significantly more computationally intensive than the MLE, this approach is less sensitive to the potential local maxima, because they are all sampled³. Note that the Bayesian method does not necessarily involve a sampling method. In its less sophisticated form, a simple maximisation (in contrast to a full sampling) of the posterior probability is performed. This is the Maximum A Posteriori (MAP) approach. This regularized maximization, in principle, outperforms the MLE in the case of informative priors, but could still be sensitive to local maxima of probability and does not enable the calculation of the evidence.

² The global likelihood requires integration over the parameters θ , which is often impossible to carry out analytically.

³ This is a limit property, i.e. when the number of samples tend towards infinity. Due to the finite number of samples, in practice it is not certain that all of the parameter space is explored.

4. Mode Parameters

In contrast to the binary star system HD 177412 (Appourchaux et al. 2015), the extraction of mode parameters from the power spectrum of HD 176465 is complicated by the overlapping frequencies of the two stars. While we have followed the fitting strategy used in previous analyses of single stars (e.g. Campante et al. 2011; Mathur et al. 2011, 2013; Appourchaux et al. 2012), extra care was required to ensure a correct fit of the power spectrum.

Initial values for the mode frequencies were obtained by scaling the solar p-mode frequencies measured by BiSON (Broomhall et al. 2009). The solar frequencies were scaled by the ratio of the large separations of HD 176465 to the Sun (Bedding & Kjeldsen 2010). To account for the different values of the small separations $\delta\nu_{0l}$ and phase offset ϵ in these stars compared to the Sun, uniform shifts were then applied to all modes of the same degree so that the scaled and shifted solar frequencies corresponded to the observed peaks in the power spectrum of HD 176465.

Several teams then used these estimates as inputs to perform a comprehensive fit of the power spectrum, including the background, for both stars simultaneously. The power spectrum of each star was modelled as a sum of Lorentzian profiles, with frequencies $\nu_{n,l}$, heights H and linewidths Γ as free parameters. Additionally, some teams also included the effect of rotation, with the rotational splitting frequency ν_s and inclination of the stellar rotation axis i as additional free parameters.

The teams differed in how they approached finding the best fit, with some using MLE (e.g. Appourchaux et al. 1998), others using the MAP method (e.g. Gaulme et al. 2009), or the MCMC method (e.g. Benomar 2008).

To identify a single set of mode parameters to be adopted in our analysis, the frequencies reported by each team were compared to find the “best” fitter that provided the smallest deviation from the average frequencies across the power spectrum. Statistical outlier rejection was performed using Peirce’s criterion (Peirce 1852; Gould 1855), as previously used in the analysis of other *Kepler* targets (Campante et al. 2011; Mathur et al. 2011; Appourchaux et al. 2012). Care was required where the frequencies of the two stars overlapped to ensure that the modes were identified with the correct star.

The “best” fitter, which used a Bayesian approach coupled with a MCMC algorithm, then performed a final analysis of the power spectrum. The two stars were fitted simultaneously in order to separate their overlapping stellar pulsations (see Fig. 1). A local fit was then performed to determine the probability of detection for each pulsation mode. A thorough description of the method and of the priors is given in Appendix A.

The fitted mode parameters are given in Table 4 for HD 176465 A and Table 5 for HD 176465 B. The fitted frequencies are shown in the échelle diagrams in Fig. 3. We show in Fig. 4 the residual power spectrum after removing the signal from HD 176465 A (middle panel) and from both stars (bottom panel). The lack of significant residual power indicates the precision of this fit.

Mode heights are shown in Fig. 5 and linewidths in Fig. 6. Figure 7 shows the mode amplitudes, defined as $\sqrt{\pi H \Gamma}$. The mode heights and amplitudes are lower than would be the case if these stars were observed separately because the oscillation signals are diluted by the presence of the other star. For the A component, the heights and amplitudes are lower by a factor of 1.8; for the B component, they are lower by a factor of 2.2.

In Fig. 6, we note that both stars have a width profile similar to the Sun, with a plateau of nearly constant linewidths around ν_{\max} . As a comparison, we have computed theoretical linewidths for the best-fitting models determined using the AST-FIT method we present in Sect. 6. The theoretical linewidths are calculated as described by Balmforth (1992) and Houdek et al. (1999), and are shown as the solid curve in Fig. 6. In general, there is good qualitative agreement between the observed and theoretical linewidths. In HD 176465 B, however, the observed linewidth drops off sharply below $\sim 3200 \mu\text{Hz}$. As a likely explanation, we note that Appourchaux et al. (2014) found widths and heights may not be accurate for low signal-to-noise modes and the Lorentzian tails of the nearby modes from the primary component may have biased the noise estimate.

The results for the inclination angles and rotational splittings are given in Fig. 8. The A component of the system has an internal average rotation period of 17.5–22.3 d and has a stellar inclination of 45.2° – 59.7° (using confidence intervals at 1σ). The B component rotation period is 16.3–19.6 d with an inclination of 44.1° – 57.9° . Within uncertainties, the two components therefore have the same inclination.

5. Non-Seismic Stellar Parameters

5.1. Orbit

Position measurements in the Washington Double Star Catalog date back to 1902 (Mason et al. 2001). Over the last century the position angle of the binary has changed by 40° , indicating a period on the order of 1000 years. The position of the secondary relative to the primary is shown in Fig. 9. Unfortunately, an insufficient fraction of the orbit has been covered to constrain the total mass. Currently the stars are separated by $\sim 1.4''$.

Table 1. Stellar properties of HD 176465 A and B

Property	HD 176465 A	HD 176465 B
H_p	8.605 ± 0.006	8.797 ± 0.007
B_T	9.193 ± 0.018	9.394 ± 0.019
V_T	8.537 ± 0.012	8.674 ± 0.014
Parallax (mas)	20.18 ± 0.74	
Distance (pc)	49.6 ± 1.8	
Radial velocity (km s^{-1})	-30.5 ± 0.4	
[Fe/H] (dex)	-0.30 ± 0.06	
ν_{\max} (μHz)	3260 ± 30	3520 ± 40
$\Delta\nu$ (μHz)	146.79 ± 0.12	155.42 ± 0.13
$\log(g/\text{cm s}^{-2})$	4.463 ± 0.005	4.492 ± 0.006
T_{eff} (K)	5830 ± 90	5740 ± 90

5.2. Spectroscopy

A spectrum of HD 176465 was obtained on 01 Apr 2010 with the ESPaDOnS spectrograph on the 3.6 m Canada-France-Hawaii Telescope. The spectrograph is fibre-fed, and light from both stars is expected to have fallen within the fibre footprint. The stars are very similar in temperature and metallicity, and so, unless the system is double-lined, distinguishing both stars in the same spectra would be difficult. The spectrum has been analysed as a single star by Bruntt et al. (2012) and Molenda-Żakowicz et al. (2013) with different spectroscopic methods. Bruntt et al. (2012) used vwa to derive the fundamental stellar parameters and elemental abundances from the spectra, finding $T_{\text{eff}} = 5755 \pm 60 \text{ K}$, $\log g = 4.48 \pm 0.03 \text{ dex}$ and $[\text{Fe}/\text{H}] = -0.30 \pm 0.06 \text{ dex}$. Molenda-Żakowicz et al. (2013) used ROTFIT, finding $T_{\text{eff}} = 5736 \pm 92 \text{ K}$, $\log g = 4.29 \pm 0.21 \text{ dex}$ and $[\text{Fe}/\text{H}] = -0.31 \pm 0.21 \text{ dex}$, and ARES+MOOG, finding $T_{\text{eff}} = 5864 \pm 68 \text{ K}$, $\log g = 4.57 \pm 0.11 \text{ dex}$ and $[\text{Fe}/\text{H}] = -0.24 \pm 0.06 \text{ dex}$.

In order to obtain separate constraints on T_{eff} and $\log g$ for the two components, we consider other, non-spectroscopic observations of the stars. We adopt the metallicity measurement of $[\text{Fe}/\text{H}] = -0.30 \pm 0.06 \text{ dex}$ by Bruntt et al. (2012) for both components. We expect both stars would have had the same initial composition because they would have formed at the same time from the same gas cloud. Effects such as gravitational settling could have subsequently led to different surface metallicities; however, because the stars have a similar mass, we consider these effects to be negligible.

5.3. Deriving individual T_{eff} and $\log g$

We have separate photometric and asteroseismic measurements of each component with which we can obtain separate constraints for each star. Separate magnitudes for each star are provided in the Hipparcos (Perryman et al. 1997) and Tycho-2 (Høg et al. 2000) catalogues, and are listed in Table 1.

From the apparent magnitudes and revised Hipparcos parallax (van Leeuwen 2007), the absolute magnitude can be determined. Using a bolometric correction, the absolute magnitude can be used to find the stellar luminosity. Since $L \propto R^2 T_{\text{eff}}^4$, we only require the radius of the star to determine the effective temperature. This final ingredient is provided by the asteroseismic scaling relation for radius,

$$\frac{R}{R_\odot} \approx \left(\frac{\nu_{\max}}{\nu_{\max,\odot}} \right) \left(\frac{\Delta\nu}{\Delta\nu_\odot} \right)^{-2} \left(\frac{T_{\text{eff}}}{T_{\text{eff},\odot}} \right)^{1/2}. \quad (5)$$

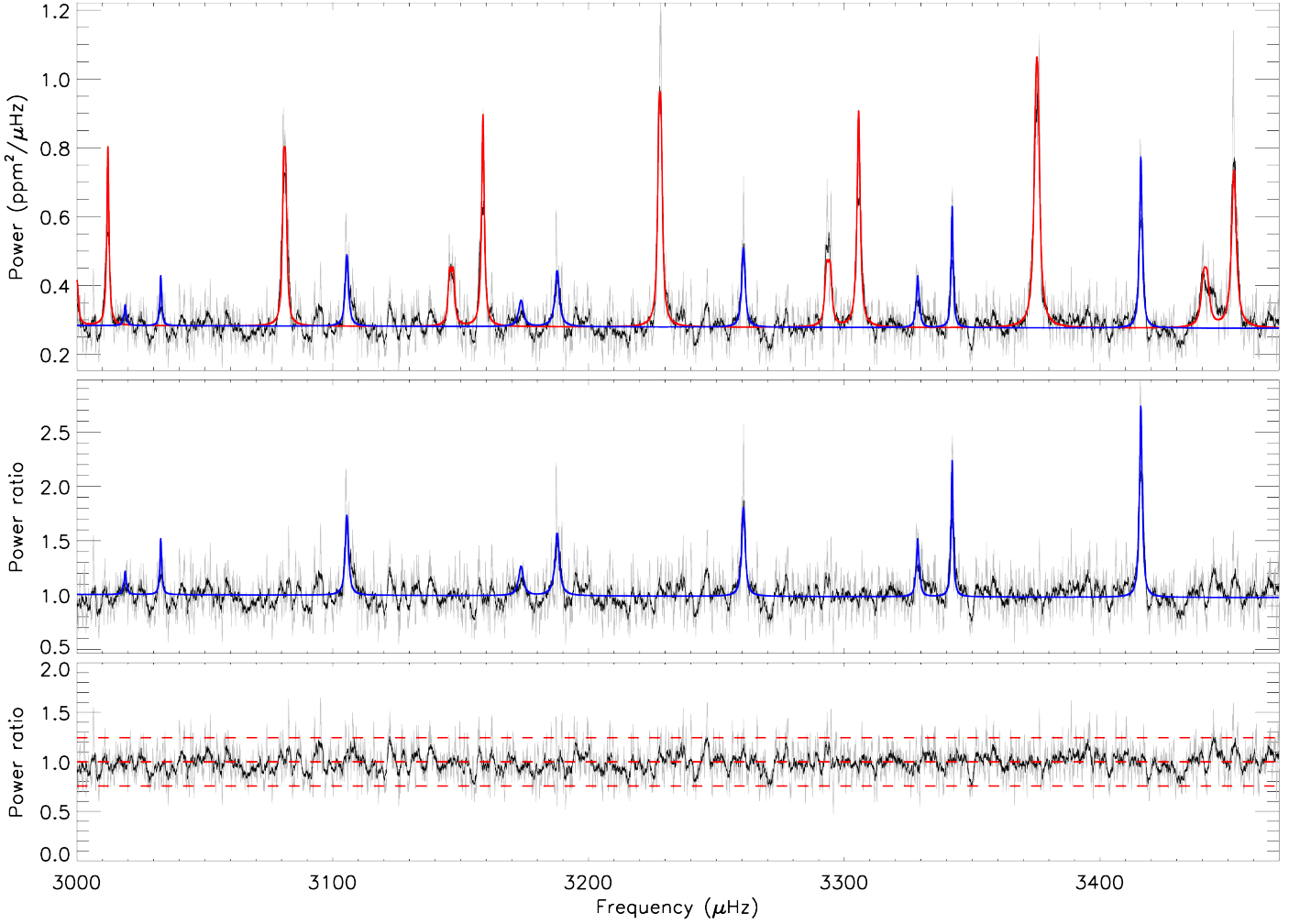


Fig. 4. Top. Smoothed power spectrum using a boxcar filter over $0.5 \mu\text{Hz}$ (grey) and $2 \mu\text{Hz}$ (black) between $3000 \mu\text{Hz}$ and $3470 \mu\text{Hz}$. Superimposed is the best fit for HD 176465 A (red) and HD 176465 B (blue). Middle. Residual power spectrum of HD 176465 B, obtained by dividing the original spectrum with the best fit of HD 176465 A. Bottom. Residual power spectrum obtained by dividing the original spectrum with the best fit for HD 176465 A and B. Data points between the lower/higher red-dashed lines have 95% probability to be due to noise for the black power spectrum.

Combined with the luminosity, we then have,

$$\frac{T_{\text{eff}}}{T_{\text{eff},\odot}} \approx \left(\frac{L}{L_{\odot}}\right)^{1/5} \left(\frac{\nu_{\text{max}}}{\nu_{\text{max},\odot}}\right)^{-2/5} \left(\frac{\Delta\nu}{\Delta\nu_{\odot}}\right)^{4/5}. \quad (6)$$

Bolometric corrections have been computed in the Hipparcos bandpass (Bessell 2000) using the Castelli models discussed by Bessell et al. (1998). The Hp -band bolometric corrections were determined by interpolating the model grid to the measured value of $B_T - V_T$, and the assumed spectroscopic values of $[\text{Fe}/\text{H}]$ and $\log g$. This bolometric correction was then applied to the absolute Hp -band magnitude to determine the bolometric magnitude of the stars, and thus the luminosity.

Values of the asteroseismic parameters were measured from the *Kepler* data. Usual methods of determining ν_{max} , such as heavily smoothing the power spectrum and fitting a Gaussian function, could not be applied in this case. This is due to the frequencies of both stars existing within the same range. Instead we have used the results of the peak-bagging to separate the frequencies from each star and fitted a Gaussian function to the mode amplitudes. The large separations, $\Delta\nu$, were derived from a linear least-squares fit to the $l=0$ frequencies. The measured asteroseismic parameters for each star are listed in Table 1.

Equation (6) was then used to provide a first estimate of T_{eff} . The bolometric correction was based on the value of $\log g$

from spectroscopy. The measurement of $\log g$ for each star was then improved using the asteroseismic scaling relation for the frequency of maximum power (Brown et al. 1991; Kjeldsen & Bedding 1995; Belkacem et al. 2011),

$$\nu_{\text{max}} \propto \nu_{\text{ac}} \propto \frac{c}{H} \propto g T_{\text{eff}}^{-1/2}, \quad (7)$$

where ν_{ac} is the acoustic cut-off frequency, c is the sound speed, $H = -(d \ln \rho / dr)^{-1}$ is the density scale height. We iterated several times, redetermining the bolometric correction for new values of $\log g$ to find updated values of T_{eff} until the values became stable.

Uncertainties in T_{eff} and $\log g$ were determined through Monte Carlo simulations, assuming Gaussian uncertainties in all input parameters. The derived quantities are included in Table 1, and are consistent with the spectroscopic values determined for the combined system.

6. Modelling

We have used four different modelling approaches to determine the properties of HD 176465 A and B using the measured oscillation frequencies determined in Sect. 4 and the non-seismic parameters determined in Sect. 5. Following Davies et al. (2014),

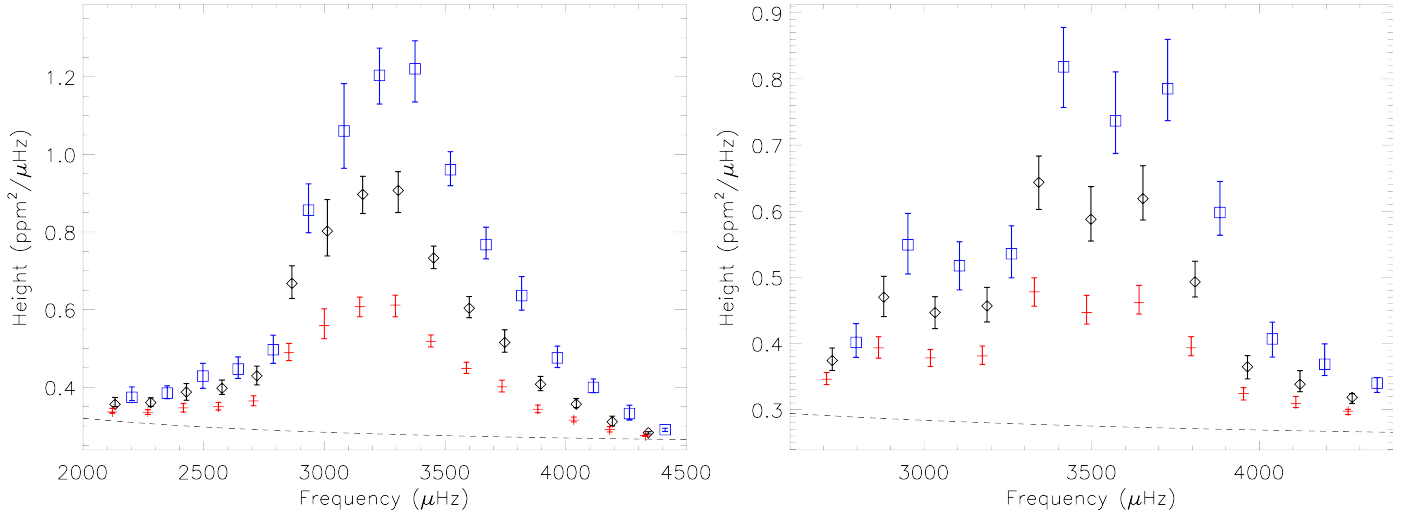


Fig. 5. Mode heights for HD 176465 A (left) and B (right). Angular degree, $l = 0, 1, 2$, of the modes are indicated by the black diamonds, blue squares, and red crosses, respectively. The dashed lines indicate the noise background.

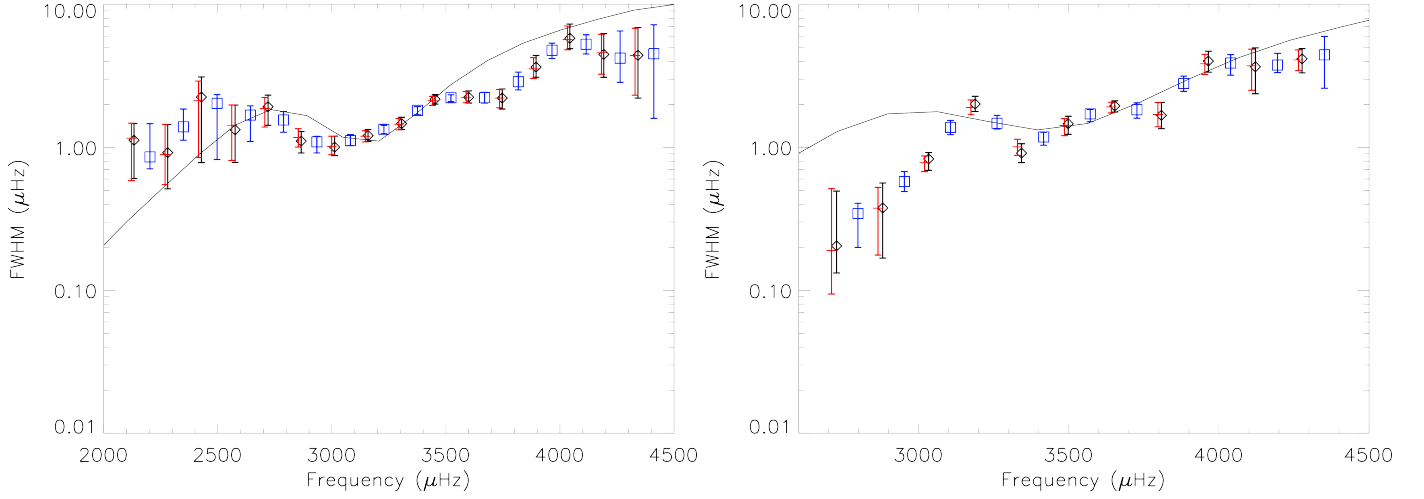


Fig. 6. Mode widths for HD 176465 A (left) and B (right). Angular degree, $l = 0, 1, 2$, of the modes are indicated by the black diamonds, blue squares, and red crosses, respectively. The solid curves show the theoretical linewidths (Houdek et al. 1999; Houdek et al., in preparation) computed from the ASTFIT models discussed in Sect. 6.

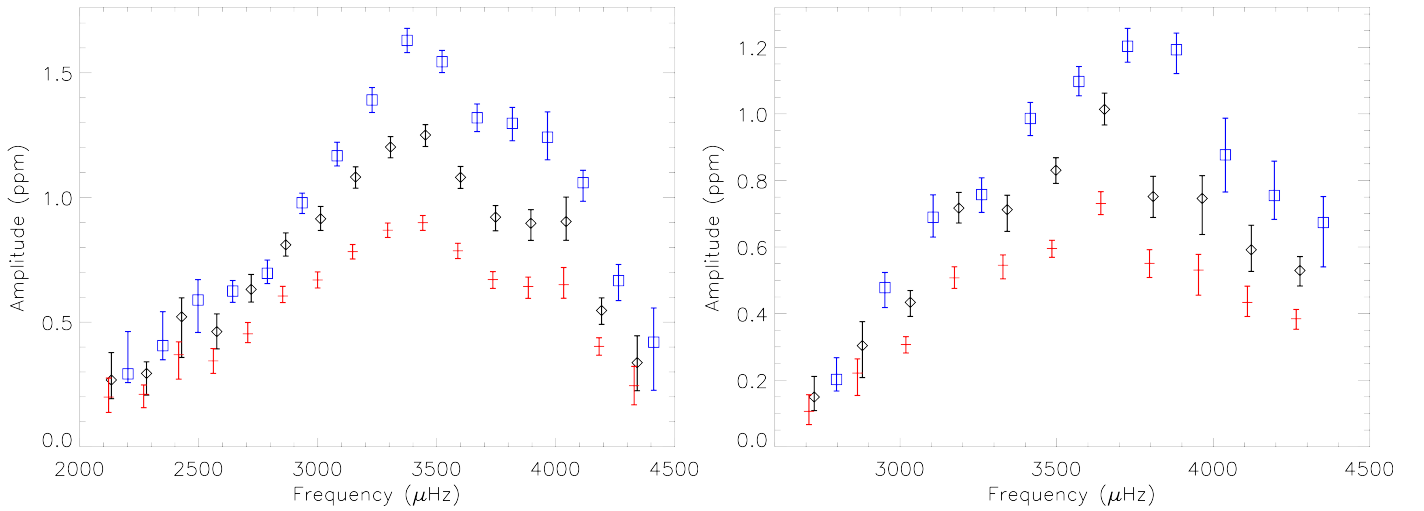


Fig. 7. Mode amplitudes for HD 176465 A (left) and B (right). Angular degree, $l = 0, 1, 2$, of the modes are indicated by the black diamonds, blue squares, and red crosses, respectively. These are defined as $\sqrt{\pi H \Gamma}$.

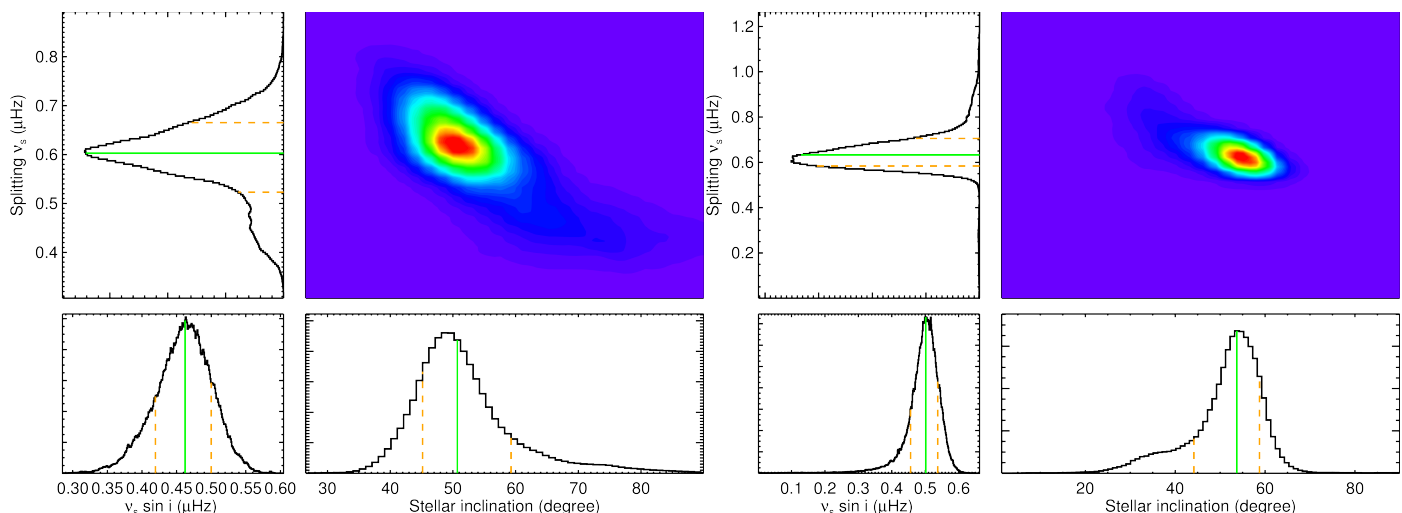


Fig. 8. Posterior distribution of the frequency splitting as a function of inclination angle for HD 176465 A (left) and B (right). The marginalized distributions for the splitting and inclination angle are shown in the histograms along each axis. The distributions for $\nu_s \sin i$ are shown in the lower-left corners. The solid green lines indicate the median value of the distributions, while the dashed orange lines indicate the 68% confidence intervals.

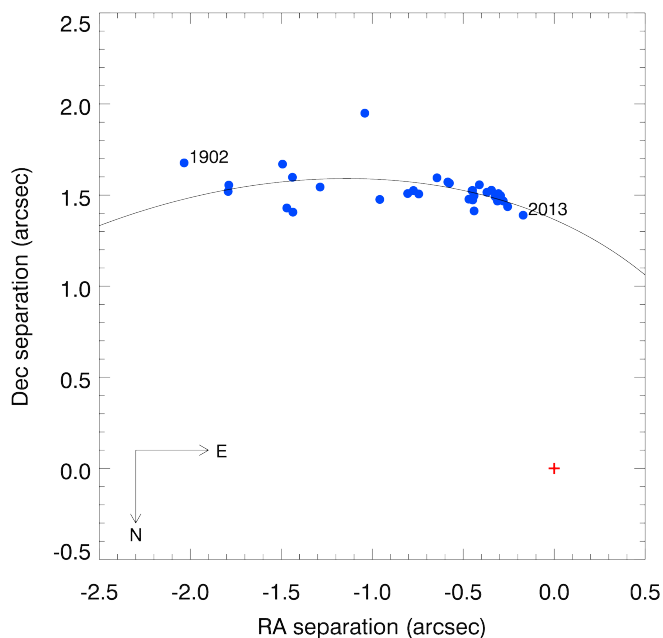


Fig. 9. Positions of the secondary component (blue circles) relative to the primary (red cross) from the Washington Double Star Catalog. The curve is an ellipse fitted to the observations.

we corrected the frequencies for the line-of-sight Doppler velocity of the system ($-30.5 \pm 0.4 \text{ km s}^{-1}$; Gontcharov 2006). Although the relative Doppler velocities of the two components is unknown, it cannot be larger than the value of $v \sin i$ determined from their combined spectra when analysed as a single star (3.0 km s^{-1} ; Bruntt et al. 2012), which we have taken into account when determining the uncertainties of the corrected frequencies. The radial-velocity-corrected frequencies are provided alongside the other mode properties in Tables 4 and 5.

Since each modelling method varies in input physics, evolutionary and pulsation code, and minimization technique, the variety of methods we employed provides an indication of the

systematic uncertainty in the determined parameters. The four methods were the Asteroseismic Modeling Portal (AMP), the ASTEC Fitting (ASTFIT) method, the Bayesian Stellar Algorithm (BASTA), and modelling with the Modules for Experiments in Stellar Astrophysics (MESA) code.

The AMP, originally introduced by Metcalfe et al. (2009), uses a parallel genetic algorithm (Metcalfe & Charbonneau 2003) to optimize the match between a set of observations and models produced by the Aarhus stellar evolution and pulsation codes (ASTEC and ADIPLS; Christensen-Dalsgaard 2008a,b). The AMP code has been in continuous development (Mathur et al. 2012; Metcalfe et al. 2014, 2015), and here we use the most recent version (Creevey et al., submitted to A&A). The models use the Grevesse & Sauval (1998) solar mixture, with the OPAL 2005 equation of state (Rogers & Nayfonov 2002), OPAL opacities at high temperatures (Iglesias & Rogers 1996) supplemented with those of Ferguson et al. (2005) at low temperatures, and NACRE nuclear reaction rates (Angulo et al. 1999, 2005).

The ASTFIT and BASTA methods are both described by Silva Aguirre et al. (2015). While both methods use the same input physics (including a solar-calibrated mixing length parameter, α), the ASTFIT method uses models calculated with ASTEC, whereas the BASTA uses models calculated with the Garching Stellar Evolution Code (GARSTEC; Weiss & Schlattl 2008). Furthermore, they differ in the asteroseismic variables that are fitted. The ASTFIT method matches individual frequencies, with surface effects corrected via a scaled function determined by frequency corrections found in the solar case, whereas the BASTA fits frequency ratios, which are relatively insensitive to surface effects (Roxburgh & Vorontsov 2003). Both ASTFIT and BASTA have assumed a linear helium-to-metal enrichment law, $\Delta Y / \Delta Z = 1.4$ on the basis of big bang nucleosynthesis primordial values ($Z_0 = 0.0$, $Y_0 = 0.248$; Steigman 2010) and initial abundances from calibration of solar models. ASTFIT adopts the Grevesse & Noels (1993) solar mixture, while BASTA uses the mixture of Grevesse & Sauval (1998).

Finally, the system was modelled using the MESA⁴ (revision 7624; Paxton et al. 2011, 2013, 2015). These stellar models used the solar mixture of Grevesse & Sauval (1998) with opacities

⁴ <http://mesa.sourceforge.net>

Table 2. Modelling results for HD 176465 A

Property	AMP	ASTFIT	BASTA	MESA1	MESA2
Mass (M_{\odot})	0.930 ± 0.04	0.952 ± 0.015	$0.960^{+0.010}_{-0.011}$	0.95 ± 0.03	0.99 ± 0.02
Radius (R_{\odot})	0.918 ± 0.015	0.927 ± 0.005	$0.928^{+0.006}_{-0.003}$	0.926 ± 0.011	0.939 ± 0.006
Age (Gyr)	3.0 ± 0.4	3.2 ± 0.5	2.8 ± 0.3	3.2 ± 0.2	3.01 ± 0.12
Z_i	0.0085 ± 0.0010	0.0103 ± 0.0010	0.011 ± 0.004	0.0102 ± 0.0009	0.0094 ± 0.0009
Y_i	0.258 ± 0.024	0.262 ± 0.003	0.265 ± 0.002	0.25 ± 0.02	0.23 ± 0.02
α	1.90 ± 0.18	1.80	1.791	1.57 ± 0.11	1.79

Table 3. Modelling results for HD 176465 B

Property	AMP	ASTFIT	BASTA	MESA1	MESA2
Mass (M_{\odot})	0.930 ± 0.02	0.92 ± 0.02	$0.929^{+0.010}_{-0.011}$	1.02 ± 0.07	0.97 ± 0.04
Radius (R_{\odot})	0.885 ± 0.006	0.883 ± 0.007	$0.886^{+0.003}_{-0.006}$	0.919 ± 0.021	0.899 ± 0.013
Age (Gyr)	2.9 ± 0.5	3.4 ± 0.9	3.2 ± 0.4	2.9 ± 0.4	3.18 ± 0.31
Z_i	0.0085 ± 0.0007	0.0096 ± 0.0011	0.011 ± 0.004	0.0124 ± 0.0015	0.0122 ± 0.0011
Y_i	0.246 ± 0.013	0.262 ± 0.003	0.265 ± 0.002	0.21 ± 0.04	0.24 ± 0.04
α	1.94 ± 0.12	1.80	1.791	2.05 ± 0.28	1.79

from the OPAL tables (Iglesias & Rogers 1996) at high temperatures and from Ferguson et al. (2005) at low temperatures, and the atmospheric structure was integrated from the photosphere to an optical depth $\tau = 10^{-4}$ using the standard grey Eddington atmosphere. Convection was described using the standard mixing-length theory (e.g. Böhm-Vitense 1958) without any convective overshooting or semiconvection. Gravitational settling was included according to the method of Thoul et al. (1994). Nuclear reactions rates were drawn from tables provided by the NACRE collaboration (Angulo et al. 1999) or, when those are unavailable, the tables by Caughlan & Fowler (1988). We also used newer rates for the specific reactions $^{14}\text{N}(p, \gamma)^{15}\text{O}$ (Imbriani et al. 2005) and $^{12}\text{C}(\alpha, \gamma)^{16}\text{O}$ (Kunz et al. 2002). Oscillation mode frequencies were computed by internal calls to ADIPLS. Model frequencies were corrected for surface effects using the two-term (or *combined*) correction described by Ball & Gizon (2014).

For a given choice of mass M , initial metal abundance Z_i , initial helium abundance Y_i and mixing-length parameter α , MESA evolved a stellar model from a pre-main-sequence model with central temperature $T_c = 9 \times 10^6$ K and found the best-fitting age and surface correction parameters for those input parameters. Starting from an initial sample of 11 guesses from grid-based modelling, the input parameters were optimized with the Nelder–Mead algorithm (Nelder & Mead 1965), accelerated with linear extrapolations of the observables as functions of the initial parameters. When further iterations failed to produce better-fitting parameters, new parameter guesses were randomly drawn uniformly from within the 1σ uncertainty region and these used to continue the Nelder–Mead simplex if the random guesses were better than any element of the simplex. Once the results appeared to have converged, a final simplex was run using the best-fitting model as the initial guess to ensure that it represented a true (local) minimum. Uncertainties were determined by selecting the model with smallest χ^2 , which we denote χ_0^2 , shrinking points with $\chi^2 > \chi_0^2 + 1$ towards the best-fitting model by rescaling their distances by $\sqrt{\chi^2 - \chi_0^2}$, and finding the minimum bounding ellipsoid around the rescaled sample.

The modelling results are presented in Tables 2 and 3 for HD 176465 A and B, respectively. The various methods agree

rather well for both stars. All methods converged on models for HD 176465 A that have a mass of $0.95 \pm 0.02 M_{\odot}$ and a radius of $0.93 \pm 0.01 R_{\odot}$. For HD 176465 B, AMP, ASTFIT and BASTA all found a mass of $0.93 \pm 0.01 M_{\odot}$ and a radius of $0.89 \pm 0.01 R_{\odot}$.

The best-fitting MESA model of HD 176465 B has a higher mass than the model of HD 176465 A, and an initial helium mass fraction Y_i significantly lower than the primordial value from standard Big Bang nucleosynthesis ($Y = 0.2482 \pm 0.0007$; Steigman 2010). A further difference between these MESA models can be noted in the mixing-length parameter, with the values for the HD 176465 A and B models being lower and higher, respectively, than the solar-calibrated value. Calibration of the mixing length against 3D models of convection suggests that neither of these behaviours is to be expected for stars so similar to the Sun (Trampedach et al. 2014).

A further set of MESA models run with the mixing-length parameter kept fixed at the solar-calibrated value (designated MESA2 in Tables 2 and 3) results in a consistent initial helium fraction for both stars and a higher mass for the primary component, as expected. However, the initial helium fraction of the best-fitting MESA2 models remain below the primordial value, which may partly explain why the masses and radii of these models are larger than those obtained with AMP, ASTFIT and BASTA. Similarly, the best-fitting AMP model of HD 176465 B has a comparable mass to the AMP model of HD 176465 A while also having a low initial helium abundance. This degeneracy between mass and helium abundance is well-known in asteroseismic modelling of solar-like oscillations (see Silva Aguirre et al. 2015). As discussed, the ASTFIT and BASTA methods have circumvented this problem by enforcing $\Delta Y / \Delta Z = 1.4$.

Significantly, although the ages of both components were not *a priori* constrained to be the same, all models agreed on the same age of both stars, 3.0 ± 0.5 Gyr.

7. Stellar Activity

In addition to solar-like oscillations, the time series of HD 176465 also shows variation on longer time scales, indicative of spot-induced rotational modulation. The periodogram, shown in Fig. 10, has a clear signal with a period of ~ 18 d.

The light curve was analysed by several teams using a variety of methods, which have been compared by Aigrain et al. (2015). García et al. (2014) reported a period value from the Q0–14 time series of 17.6 ± 2.3 d. McQuillan et al. (2014) found a period of 19.2 ± 0.8 d, although this period did not meet their significance criterion, which can be attributed to the rotational modulation not being particularly stable. This is probably due to the spots being small or short-lived, but it is possible that beating between two closely-spaced frequencies, corresponding to the rotation periods of each star, may also contribute. The periods measured by García et al. (2014) and McQuillan et al. (2014) are consistent with the values determined from the rotational splitting of non-radial modes in Sect. 4 for both stars.

Since the rotation rates of stars are known to decrease as they age, the rotation period may be used to provide an estimate of the age using suitably calibrated gyrochronology relations (Skumanich 1972; Barnes 2010; Epstein & Pinsonneault 2014). Using the gyrochronology relation of Barnes (2010), and using $P_{\text{rot}} = 18 \pm 2$ d, we find ages of $2.5^{+0.6}_{-0.5}$ and $2.1^{+0.5}_{-0.4}$ Gyr for the A and B components, respectively. García et al. (2014) calibrated a simpler gyrochronology relation between age and period for a sample of stars with asteroseismic ages; using this relation we find an age of $3.2^{+1.2}_{-0.8}$ Gyr.

These gyrochronological ages are in good agreement with the asteroseismic ages obtained in Sect. 6. This is in contrast to the recent study by Angus et al. (2015), who found a significant disagreement between asteroseismic and gyrochronological ages in *Kepler* field stars. However, van Saders et al. (2016) have explained that disagreement as being a result of weakened magnetic braking in old stars. Since the HD 176465 system is still relatively young, the standard gyrochronology relations still appear to hold.

García et al. (2014) also investigated the level of photospheric magnetic activity in HD 176465. They computed the standard deviation of the time series, which has been used as a photometric magnetic activity index, denoted S_{ph} (García et al. 2010; Mathur et al. 2014). García et al. (2014) found $S_{\text{ph}} = 248 \pm 4$ ppm, which is close to the value for the Sun during its maximum activity of Cycle 23, as measured from VIRGO/SPM (see Mathur et al. 2014). Furthermore, the S_{ph} obtained is a lower limit since the inclination angle is $\sim 50^\circ$. Although it is difficult to distinguish between the contributions of each star, it is likely that this measurement represents a higher photospheric magnetic activity than the Sun during the last activity maximum.

Additionally, HD 176465 was amongst a sample of *Kepler* targets monitored for excess flux in the Ca H and K lines with the Fibre-fed Echelle Spectrograph (FIES) on the Nordic Optical Telescope by Karoff et al. (2013), although it was dropped from their analysis due to its binary nature. Excess flux in the cores of these lines arises from magnetic sources (see Schrijver et al. 1989). Analysing these FIES spectra following the methods of Karoff et al. (2013), we find the excess flux to be $\Delta\mathcal{F}_{\text{Ca}} = 6.02 \pm 0.28$, from which we derive the Mount Wilson S index, 0.170 ± 0.003 . As for the photometric measurement of activity, both of these values reflect a relatively high activity level.

8. Conclusions

Situated at only 49.6 ± 1.8 pc, the HD 176465 binary system is sufficiently bright to reveal solar-like oscillations in both components. Only four other systems, namely α Cen, 16 Cyg, HD 177412, and HD 176071, are known to share this property. With both stars having solar-like oscillations with $\nu_{\text{max}} \approx$

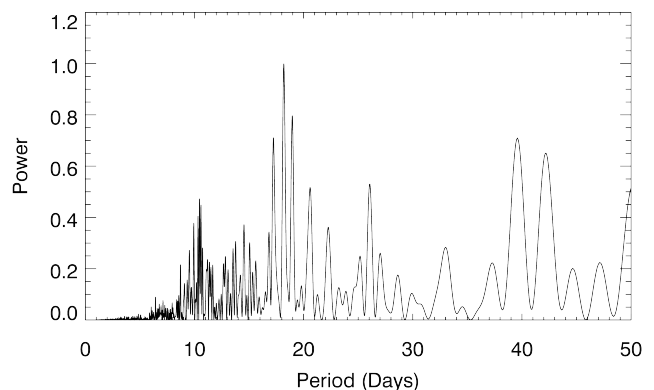


Fig. 10. Periodogram of the long cadence data showing evidence of rotational modulation at a period of ~ 18 days.

$3500 \mu\text{Hz}$ and $\Delta\nu \approx 150 \mu\text{Hz}$, and with an effective temperature of ≈ 5700 K, the system is comprised of two similar solar analogues.

Detailed modelling of the power spectrum has enabled us to extract the frequencies, linewidths and heights of 45 modes for HD 176465 A, and 25 modes for HD 176465 B, up to an angular degree of $l = 2$ and with a statistical significance greater than 75%.

The rotational splittings of the non-radial modes reveal both stars to have a similar rotation period of ~ 18 d and inclination of $\sim 50^\circ$. This rotation period is in agreement with that determined from the rotational modulation caused by the presence of starspots. Gyrochronology relations imply an age of ~ 3 Gyr.

Precise estimates for the fundamental stellar parameters have been derived through detailed modelling of both stars. The four methods used to model these stars agree on the stellar properties in almost all cases. The masses of the stars are $M_A = 0.95 \pm 0.02 M_\odot$ and $M_B = 0.93 \pm 0.01 M_\odot$, and their radii are $R_A = 0.93 \pm 0.01 R_\odot$ and $R_B = 0.89 \pm 0.01 R_\odot$. From the modelling, the ages of both stars are found to be 3.0 ± 0.5 Gyrs, in agreement with the gyrochronological value, and consistent with a synchronous formation.

While main-sequence systems such as this are rare, they provide important tests of stellar structure and evolution, and of asteroseismology. Miglio et al. (2014) predicted there should be more such systems amongst the many red giants observed by *Kepler*. The absence in the literature of systems with clear oscillations in two red giants is possibly a consequence of the difficulty in recognising the typical pattern of solar-like oscillations when modes overlap in frequency. While the overlapping modes of HD 176465 have presented a (thus far) unique challenge in determining mode parameters, overlapping modes of red giants, with their many mixed $l = 1$ modes, will present a far greater challenge. Despite these challenges, such systems will provide further tests of stellar structure and evolution when they are found, just as systems with a single oscillating red giant have already (e.g. Hekker et al. 2010b; Frandsen et al. 2013; Gaulme et al. 2013, 2014; Beck et al. 2014; Rawls et al. 2016). With the future missions *TESS* (Ricker et al. 2015; Campante et al. 2016) and *PLATO* (Rauer et al. 2014) to provide asteroseismic data for many more systems, there will be good opportunities to find more such asteroseismic binary systems.

Acknowledgements. The authors gratefully acknowledge the *Kepler* Science Team and all those who have contributed to the *Kepler Mission* for their tireless efforts which have made these results possible. Funding for the *Kepler Mission* was provided by NASA's Science Mission Directorate. Funding for the Stellar

Astrophysics Centre is provided by The Danish National Research Foundation (Grant agreement no.: DNR106). The research was supported by the ASTERISK project (ASTERoseismic Investigations with SONG and *Kepler*) funded by the European Research Council (Grant agreement no.: 267864). TRW and VSA acknowledge support from the Villum Foundation (research grant 10118) and the Instrument Centre for Danish Astrophysics. CK also acknowledges the support of the Villum Foundation. OB, LG and MB acknowledge support by the Center for Space Science at the NYU Abu Dhabi Institute under grant G1502. WHB acknowledges research funding by Deutsche Forschungsgemeinschaft (DFG) under grant SFB 963/1 “Astrophysical flow instabilities and turbulence” (Project A18). GRD, WJC, TLC, and YE acknowledge the support of the UK Science and Technology Facilities Council (STFC). RAG, BM, and D. Salabert acknowledges funding from the CNES and the ANR (Agence Nationale de la Recherche, France) program IDEE (n ANR-12-BS05-0008) “Interaction Des Étoiles et des Exoplanètes”. The research leading to the presented results has received funding from the European Research Council under the European Community’s Seventh Framework Programme (FP7/2007-2013) / ERC grant agreement no 338251 (StellarAges). R. Howe acknowledges computing support from the National Solar Observatory. DH acknowledges support by the Australian Research Council’s Discovery Projects funding scheme (project number DE140101364) and support by the National Aeronautics and Space Administration under Grant NNX14AB92G issued through the Kepler Participating Scientist Program. SM acknowledges support from the NASA grant NNX12AE17G. This research made use of NASA’s Astrophysics Data System and the SIMBAD database, operated at CDS, Strasbourg, France. TSM acknowledges NASA grants NNX13AE91G and NNX15AF13G. Computational time at the Texas Advanced Computing Center was provided through XSEDE allocation TG-AST090107.

References

- Aigrain, S., Llama, J., Ceillier, T., et al. 2015, *MNRAS*, 450, 3211
- Anderson, E. R., Duvall, Jr., T. L., & Jefferies, S. M. 1990, *ApJ*, 364, 699
- Angulo, C., Arnould, M., Rayet, M., et al. 1999, *Nuclear Physics A*, 656, 3
- Angulo, C., Champagne, A. E., & Trautvetter, H.-P. 2005, *Nuclear Physics A*, 758, 391
- Angus, R., Aigrain, S., Foreman-Mackey, D., & McQuillan, A. 2015, *MNRAS*, 450, 1787
- Appourchaux, T., Antia, H. M., Ball, W., et al. 2015, *A&A*, 582, A25
- Appourchaux, T., Antia, H. M., Benomar, O., et al. 2014, *A&A*, 566, A20
- Appourchaux, T., Chaplin, W. J., García, R. A., et al. 2012, *A&A*, 543, A54
- Appourchaux, T., Gizon, L., & Rabello-Soares, M.-C. 1998, *A&AS*, 132, 107
- Ball, W. H. & Gizon, L. 2014, *A&A*, 568, A123
- Balmforth, N. J. 1992, *MNRAS*, 255, 603
- Barnes, S. A. 2010, *ApJ*, 722, 222
- Bazot, M., Bouchy, F., Kjeldsen, H., et al. 2007, *A&A*, 470, 295
- Beck, P. G., Hambleton, K., Vos, J., et al. 2014, *A&A*, 564, A36
- Bedding, T. R. & Kjeldsen, H. 2010, *Communications in Asteroseismology*, 161, 3
- Bedding, T. R., Kjeldsen, H., Butler, R. P., et al. 2004, *ApJ*, 614, 380
- Belkacem, K., Goupil, M. J., Dupret, M. A., et al. 2011, *A&A*, 530, A142
- Benomar, O. 2008, *Communications in Asteroseismology*, 157, 98
- Benomar, O., Appourchaux, T., & Baudin, F. 2009a, *A&A*, 506, 15
- Benomar, O., Baudin, F., Campante, T. L., et al. 2009b, *A&A*, 507, L13
- Benomar, O., Baudin, F., Chaplin, W. J., Elsworth, Y., & Appourchaux, T. 2012, *MNRAS*, 420, 2178
- Bessell, M. S. 2000, *PASP*, 112, 961
- Bessell, M. S., Castelli, F., & Plez, B. 1998, *A&A*, 333, 231
- Böhm-Vitense, E. 1958, *ZAp*, 46, 108
- Bouchy, F. & Carrier, F. 2002, *A&A*, 390, 205
- Broomhall, A., Chaplin, W. J., Davies, G. R., et al. 2009, *MNRAS*, 396, L100
- Brown, T. M., Gilliland, R. L., Noyes, R. W., & Ramsey, L. W. 1991, *ApJ*, 368, 599
- Bruntt, H., Basu, S., Smalley, B., et al. 2012, *MNRAS*, 423, 122
- Campante, T. L., Handberg, R., Mathur, S., et al. 2011, *A&A*, 534, A6
- Campante, T. L., Karoff, C., Chaplin, W. J., et al. 2010, *MNRAS*, 1125
- Campante, T. L., Schofield, M., Kuszewicz, J. S., et al. 2016, *ApJ*, in press
- Carrier, F. & Bourban, G. 2003, *A&A*, 406, L23
- Caughlan, G. R. & Fowler, W. A. 1988, *Atomic Data and Nuclear Data Tables*, 40, 283
- Chaplin, W. J., Basu, S., Huber, D., et al. 2014, *ApJS*, 210, 1
- Chaplin, W. J., Elsworth, Y., Howe, R., et al. 1996, *MNRAS*, 280, 849
- Chaplin, W. J., Kjeldsen, H., Christensen-Dalsgaard, J., et al. 2011, *Science*, 332, 213
- Christensen-Dalsgaard, J. 1984, in *Space Research in Stellar Activity and Variability*, ed. A. Manganey & F. Praderie, 11–46
- Christensen-Dalsgaard, J. 2008a, *Ap&SS*, 316, 13
- Christensen-Dalsgaard, J. 2008b, *Ap&SS*, 316, 113
- Christensen-Dalsgaard, J., Arentoft, T., Brown, T. M., et al. 2008, *Journal of Physics Conference Series*, 118, 012039
- Corsaro, E. & De Ridder, J. 2014, *A&A*, 571, A71
- Davies, G. R., Chaplin, W. J., Farr, W. M., et al. 2015, *MNRAS*, 446, 2959
- Davies, G. R., Handberg, R., Miglio, A., et al. 2014, *MNRAS*, 445, L94
- Epstein, C. R. & Pinsonneault, M. H. 2014, *ApJ*, 780, 159
- Ferguson, J. W., Alexander, D. R., Allard, F., et al. 2005, *ApJ*, 623, 585
- Fletcher, S. T., Chaplin, W. J., Elsworth, Y., Schou, J., & Buzasi, D. 2006, *MNRAS*, 371, 935
- Frandsen, S., Lehmann, H., Hekker, S., et al. 2013, *A&A*, 556, A138
- García, R. A., Ceillier, T., Salabert, D., et al. 2014, *A&A*, 572, A34
- García, R. A., Hekker, S., Stello, D., et al. 2011, *MNRAS*, 414, L6
- García, R. A., Mathur, S., Salabert, D., et al. 2010, *Science*, 329, 1032
- Gaulme, P., Appourchaux, T., & Boumier, P. 2009, *A&A*, 506, 7
- Gaulme, P., Jackiewicz, J., Appourchaux, T., & Mosser, B. 2014, *ApJ*, 785, 5
- Gaulme, P., McKeever, J., Rawls, M. L., et al. 2013, *ApJ*, 767, 82
- Gilliland, R. L., Brown, T. M., Christensen-Dalsgaard, J., et al. 2010a, *PASP*, 122, 131
- Gilliland, R. L., Jenkins, J. M., Borucki, W. J., et al. 2010b, *ApJ*, 713, L160
- Gontcharov, G. A. 2006, *Astronomy Letters*, 32, 759
- Gough, D. O. 1986, in *Hydrodynamic and Magnetodynamic Problems in the Sun and Stars*, ed. Y. Osaki, 117
- Gould, B. A. 1855, *AJ*, 4, 81
- Grevesse, N. & Noels, A. 1993, in *Origin and Evolution of the Elements*, ed. S. Kubono & T. Kajino, 14
- Grevesse, N. & Sauval, A. J. 1998, *Space Sci. Rev.*, 85, 161
- Handberg, R. & Campante, T. L. 2011, *A&A*, 527, A56
- Harvey, J. 1985, *ESA SP*, 235, 199
- Hekker, S., Broomhall, A., Chaplin, W. J., et al. 2010a, *MNRAS*, 402, 2049
- Hekker, S., Debosscher, J., Huber, D., et al. 2010b, *ApJ*, 713, L187
- Høg, E., Fabricius, C., Makarov, V. V., et al. 2000, *A&A*, 355, L27
- Houdek, G., Balmforth, N. J., Christensen-Dalsgaard, J., & Gough, D. O. 1999, *A&A*, 351, 582
- Huber, D., Stello, D., Bedding, T. R., et al. 2009, *Communications in Asteroseismology*, 160, 74
- Iglesias, C. A. & Rogers, F. J. 1996, *ApJ*, 464, 943
- Imbriani, G., Costantini, H., Formicola, A., et al. 2005, *European Physical Journal A*, 25, 455
- Jeffreys, H. 1961, *Theory of Probability*, 3rd edn. (Oxford, England: Oxford)
- Jenkins, J. M., Caldwell, D. A., Chandrasekaran, H., et al. 2010, *ApJ*, 713, L87
- Karoff, C. 2012, *MNRAS*, 421, 3170
- Karoff, C., Campante, T. L., & Chaplin, W. J. 2010, *ArXiv*: 1003.4167
- Karoff, C., Metcalfe, T. S., Chaplin, W. J., et al. 2013, *MNRAS*, 433, 3227
- Keen, M. A., Bedding, T. R., Murphy, S. J., et al. 2015, *MNRAS*, 454, 1792
- Kjeldsen, H. & Bedding, T. R. 1995, *A&A*, 293, 87
- Kjeldsen, H., Bedding, T. R., Butler, R. P., et al. 2005, *ApJ*, 635, 1281
- Kunz, R., Fey, M., Jaeger, M., et al. 2002, *ApJ*, 567, 643
- Mason, B. D., Wycoff, G. L., Hartkopf, W. I., Douglass, G. G., & Worley, C. E. 2001, *AJ*, 122, 3466
- Mathur, S., Bruntt, H., Catala, C., et al. 2013, *A&A*, 549, A12
- Mathur, S., García, R. A., Ballot, J., et al. 2014, *A&A*, 562, A124
- Mathur, S., García, R. A., Régulo, C., et al. 2010, *A&A*, 511, A46
- Mathur, S., Handberg, R., Campante, T. L., et al. 2011, *ApJ*, 733, 95
- Mathur, S., Metcalfe, T. S., Woitaszek, M., et al. 2012, *ApJ*, 749, 152
- McQuillan, A., Mazeh, T., & Aigrain, S. 2014, *ApJS*, 211, 24
- Metcalfe, T. S., Chaplin, W. J., Appourchaux, T., et al. 2012, *ApJ*, 748, L10
- Metcalfe, T. S. & Charbonneau, P. 2003, *Journal of Computational Physics*, 185, 176
- Metcalfe, T. S., Creevey, O. L., & Christensen-Dalsgaard, J. 2009, *ApJ*, 699, 373
- Metcalfe, T. S., Creevey, O. L., & Davies, G. R. 2015, *ApJ*, 811, L37
- Metcalfe, T. S., Creevey, O. L., Doğan, G., et al. 2014, *ApJS*, 214, 27
- Michel, E., Baglin, A., Auvergne, M., et al. 2008, *Science*, 322, 558
- Miglio, A., Chaplin, W. J., Farmer, R., et al. 2014, *ApJ*, 784, L3
- Molenda-Zakowicz, J., Sousa, S. G., Frasca, A., et al. 2013, *MNRAS*, 434, 1422
- Mosser, B. & Appourchaux, T. 2009, *A&A*, 508, 877
- Murphy, S. J., Bedding, T. R., Shibahashi, H., Kurtz, D. W., & Kjeldsen, H. 2014, *MNRAS*, 441, 2515
- Nelder, J. A. & Mead, R. 1965, *The Computer Journal*, 7, 308
- Paxton, B., Bildsten, L., Dotter, A., et al. 2011, *ApJS*, 192, 3
- Paxton, B., Cantiello, M., Arras, P., et al. 2013, *ApJS*, 208, 4
- Paxton, B., Marchant, P., Schwab, J., et al. 2015, *ApJS*, 220, 15
- Pearce, B. 1852, *AJ*, 2, 161
- Perryman, M. A. C., Lindegren, L., Kovalevsky, J., et al. 1997, *A&A*, 323
- Rauer, H., Catala, C., Aerts, C., et al. 2014, *Experimental Astronomy*, 38, 249
- Rawls, M. L., Gaulme, P., McKeever, J., et al. 2016, *ApJ*, 818, 108
- Ricker, G. R., Winn, J. N., Vanderspek, R., et al. 2015, *Journal of Astronomical Telescopes, Instruments, and Systems*, 1, 014003
- Rogers, F. J. & Nayfonov, A. 2002, *ApJ*, 576, 1064
- Roxburgh, I. W. 2009, *A&A*, 506, 435
- Roxburgh, I. W. & Vorontsov, S. V. 2003, *A&A*, 411, 215

- Schmid, V. S., Tkachenko, A., Aerts, C., et al. 2015, *A&A*, 584, A35
- Schrijver, C. J., Dobson, A. K., & Radick, R. R. 1989, *ApJ*, 341, 1035
- Silva Aguirre, V., Davies, G. R., Basu, S., et al. 2015, *MNRAS*, 452, 2127
- Skumanich, A. 1972, *ApJ*, 171, 565
- Steigman, G. 2010, *J. Cosmology Astropart. Phys.*, 4, 029
- Stello, D., Chaplin, W. J., Basu, S., Elsworth, Y., & Bedding, T. R. 2009, *MNRAS*, 400, L80
- Tassoul, M. 1980, *ApJS*, 43, 469
- Thoul, A. A., Bahcall, J. N., & Loeb, A. 1994, *ApJ*, 421, 828
- Trampedach, R., Stein, R. F., Christensen-Dalsgaard, J., Nordlund, Å., & Asplund, M. 2014, *MNRAS*, 445, 4366
- Ulrich, R. K. 1986, *ApJ*, 306, L37
- Urban, S. E., Corbin, T. E., Wycoff, G. L., et al. 1998, *AJ*, 115, 1212
- van Leeuwen, F. 2007, *A&A*, 474, 653
- van Saders, J. L., Ceillier, T., Metcalfe, T. S., et al. 2016, *Nature*, 529, 181
- Vandakurov, Y. V. 1967, *AZh*, 44, 786, (English translation: *Soviet Astronomy* *AJ*, 11, 630)
- Weiss, A. & Schlattl, H. 2008, *Ap&SS*, 316, 99
- White, T. R., Bedding, T. R., Gruberbauer, M., et al. 2012, *ApJ*, 751, L36

Table 4. Fitted mode parameters of HD 176465 A

n	ℓ	Frequency (μHz)	RV Corr. Freq. (μHz)	Height ($\text{ppm}^2/\mu\text{Hz}$)	Linewidth (μHz)	Amplitude (ppm)	$P(M_{\text{mode}} y)$ %
12	2	2121.39 \pm 1.67	2121.18 \pm 1.67	0.023 $^{+0.010}_{-0.004}$	1.16 $^{+0.32}_{-0.58}$	0.20 $^{+0.08}_{-0.06}$	84.0
13	0	2132.67 \pm 0.61	2132.45 \pm 0.61	0.043 $^{+0.018}_{-0.006}$	1.12 $^{+0.35}_{-0.52}$	0.27 $^{+0.11}_{-0.08}$	99.8
	1	2202.44 \pm 0.39	2202.22 \pm 0.39	0.065 $^{+0.027}_{-0.007}$	0.86 $^{+0.61}_{-0.15}$	0.29 $^{+0.17}_{-0.04}$	80.3
	2	2268.74 \pm 1.17	2268.51 \pm 1.17	0.029 $^{+0.007}_{-0.006}$	0.89 $^{+0.56}_{-0.35}$	0.21 $^{+0.04}_{-0.05}$	79.5
14	0	2280.58 \pm 0.90	2280.34 \pm 0.90	0.054 $^{+0.013}_{-0.010}$	0.92 $^{+0.53}_{-0.41}$	0.29 $^{+0.02}_{-0.09}$	96.2
	1	2348.98 \pm 0.24	2348.74 \pm 0.24	0.082 $^{+0.019}_{-0.015}$	1.39 $^{+0.47}_{-0.27}$	0.41 $^{+0.14}_{-0.06}$	83.4
	2	2415.63 \pm 1.97	2415.38 \pm 1.97	0.047 $^{+0.012}_{-0.012}$	2.12 $^{+0.79}_{-1.28}$	0.37 $^{+0.05}_{-0.10}$	18.4
15	0	2428.06 \pm 0.38	2427.81 \pm 0.38	0.087 $^{+0.022}_{-0.021}$	2.25 $^{+0.86}_{-1.47}$	0.52 $^{+0.08}_{-0.16}$	96.4
	1	2496.73 \pm 0.33	2496.48 \pm 0.33	0.131 $^{+0.034}_{-0.032}$	2.03 $^{+0.31}_{-1.21}$	0.59 $^{+0.08}_{-0.13}$	100
	2	2561.06 \pm 1.65	2560.80 \pm 1.65	0.055 $^{+0.012}_{-0.009}$	1.43 $^{+0.56}_{-0.62}$	0.34 $^{+0.05}_{-0.05}$	39.3
16	0	2575.83 \pm 0.83	2575.57 \pm 0.83	0.102 $^{+0.021}_{-0.017}$	1.33 $^{+0.65}_{-0.55}$	0.46 $^{+0.07}_{-0.07}$	84.2
	1	2642.66 \pm 0.10	2642.39 \pm 0.10	0.154 $^{+0.032}_{-0.025}$	1.68 $^{+0.27}_{-0.59}$	0.62 $^{+0.04}_{-0.05}$	100
	2	2706.15 \pm 0.74	2705.87 \pm 0.74	0.074 $^{+0.014}_{-0.013}$	1.87 $^{+0.37}_{-0.49}$	0.45 $^{+0.05}_{-0.04}$	98.0
17	0	2720.12 \pm 0.28	2719.84 \pm 0.28	0.138 $^{+0.026}_{-0.024}$	1.92 $^{+0.40}_{-0.50}$	0.63 $^{+0.06}_{-0.05}$	100
	1	2788.08 \pm 0.36	2787.80 \pm 0.36	0.208 $^{+0.038}_{-0.036}$	1.56 $^{+0.23}_{-0.28}$	0.70 $^{+0.05}_{-0.04}$	100
	2	2852.75 \pm 0.38	2852.46 \pm 0.38	0.202 $^{+0.024}_{-0.021}$	1.17 $^{+0.18}_{-0.17}$	0.60 $^{+0.04}_{-0.03}$	99.6
18	0	2865.49 \pm 0.09	2865.19 \pm 0.10	0.381 $^{+0.046}_{-0.039}$	1.11 $^{+0.19}_{-0.20}$	0.81 $^{+0.05}_{-0.04}$	100
	1	2934.23 \pm 0.12	2933.93 \pm 0.12	0.571 $^{+0.068}_{-0.059}$	1.09 $^{+0.11}_{-0.18}$	0.98 $^{+0.04}_{-0.04}$	100
	2	2999.34 \pm 0.22	2999.03 \pm 0.22	0.275 $^{+0.044}_{-0.034}$	1.02 $^{+0.19}_{-0.13}$	0.67 $^{+0.03}_{-0.03}$	100
19	0	3012.10 \pm 0.11	3011.79 \pm 0.11	0.519 $^{+0.082}_{-0.065}$	1.01 $^{+0.20}_{-0.13}$	0.91 $^{+0.05}_{-0.05}$	100
	1	3081.19 \pm 0.10	3080.88 \pm 0.11	0.778 $^{+0.122}_{-0.097}$	1.11 $^{+0.12}_{-0.09}$	1.17 $^{+0.05}_{-0.04}$	100
	2	3146.38 \pm 0.21	3146.06 \pm 0.21	0.327 $^{+0.025}_{-0.027}$	1.20 $^{+0.11}_{-0.11}$	0.78 $^{+0.03}_{-0.03}$	100
20	0	3158.74 \pm 0.02	3158.41 \pm 0.04	0.620 $^{+0.047}_{-0.050}$	1.21 $^{+0.13}_{-0.11}$	1.08 $^{+0.04}_{-0.04}$	100
	1	3227.97 \pm 0.09	3227.64 \pm 0.09	0.924 $^{+0.070}_{-0.074}$	1.34 $^{+0.09}_{-0.10}$	1.39 $^{+0.05}_{-0.05}$	100
	2	3293.79 \pm 0.17	3293.45 \pm 0.17	0.333 $^{+0.026}_{-0.031}$	1.45 $^{+0.15}_{-0.13}$	0.87 $^{+0.03}_{-0.03}$	100
21	0	3305.62 \pm 0.08	3305.28 \pm 0.08	0.629 $^{+0.049}_{-0.058}$	1.47 $^{+0.16}_{-0.14}$	1.20 $^{+0.04}_{-0.04}$	100
	1	3375.32 \pm 0.10	3374.97 \pm 0.10	0.944 $^{+0.073}_{-0.086}$	1.82 $^{+0.12}_{-0.13}$	1.63 $^{+0.05}_{-0.05}$	100
	2	3441.16 \pm 0.36	3440.81 \pm 0.35	0.242 $^{+0.017}_{-0.015}$	2.12 $^{+0.16}_{-0.16}$	0.90 $^{+0.03}_{-0.03}$	100
22	0	3452.35 \pm 0.11	3452.00 \pm 0.11	0.457 $^{+0.031}_{-0.028}$	2.17 $^{+0.17}_{-0.17}$	1.25 $^{+0.04}_{-0.05}$	100
	1	3522.07 \pm 0.14	3521.72 \pm 0.14	0.686 $^{+0.047}_{-0.042}$	2.22 $^{+0.11}_{-0.14}$	1.54 $^{+0.05}_{-0.04}$	100
	2	3588.47 \pm 0.26	3588.10 \pm 0.26	0.175 $^{+0.016}_{-0.014}$	2.24 $^{+0.22}_{-0.19}$	0.79 $^{+0.03}_{-0.03}$	100
23	0	3599.69 \pm 0.13	3599.32 \pm 0.14	0.330 $^{+0.030}_{-0.025}$	2.24 $^{+0.25}_{-0.21}$	1.08 $^{+0.04}_{-0.04}$	100
	1	3669.46 \pm 0.16	3669.08 \pm 0.16	0.495 $^{+0.045}_{-0.037}$	2.23 $^{+0.21}_{-0.19}$	1.32 $^{+0.06}_{-0.06}$	100
	2	3735.42 \pm 0.63	3735.04 \pm 0.63	0.129 $^{+0.018}_{-0.014}$	2.21 $^{+0.33}_{-0.33}$	0.67 $^{+0.03}_{-0.04}$	100
24	0	3746.85 \pm 0.16	3746.47 \pm 0.16	0.243 $^{+0.033}_{-0.025}$	2.21 $^{+0.35}_{-0.36}$	0.92 $^{+0.05}_{-0.05}$	100
	1	3817.25 \pm 0.24	3816.86 \pm 0.24	0.365 $^{+0.049}_{-0.038}$	2.88 $^{+0.48}_{-0.36}$	1.30 $^{+0.06}_{-0.07}$	100
	2	3884.21 \pm 1.72	3883.81 \pm 1.72	0.073 $^{+0.011}_{-0.009}$	3.54 $^{+0.71}_{-0.51}$	0.64 $^{+0.04}_{-0.05}$	99.7
25	0	3895.17 \pm 0.18	3894.77 \pm 0.18	0.137 $^{+0.021}_{-0.017}$	3.64 $^{+0.76}_{-0.55}$	0.90 $^{+0.05}_{-0.07}$	100
	1	3965.06 \pm 0.40	3964.65 \pm 0.40	0.206 $^{+0.031}_{-0.026}$	4.78 $^{+0.59}_{-0.60}$	1.24 $^{+0.10}_{-0.09}$	100
	2	4033.13 \pm 1.44	4032.72 \pm 1.44	0.047 $^{+0.008}_{-0.005}$	5.67 $^{+1.40}_{-0.86}$	0.65 $^{+0.07}_{-0.05}$	99.3
26	0	4043.26 \pm 0.02	4042.85 \pm 0.05	0.088 $^{+0.015}_{-0.010}$	5.80 $^{+1.49}_{-0.90}$	0.90 $^{+0.10}_{-0.08}$	100
	1	4114.50 \pm 0.50	4114.08 \pm 0.50	0.131 $^{+0.022}_{-0.014}$	5.26 $^{+0.87}_{-0.77}$	1.06 $^{+0.05}_{-0.07}$	100
	2	4181.86 \pm 0.89	4181.43 \pm 0.89	0.023 $^{+0.008}_{-0.006}$	4.59 $^{+1.60}_{-1.35}$	0.40 $^{+0.03}_{-0.04}$	81.2
27	0	4192.29 \pm 0.46	4191.86 \pm 0.46	0.044 $^{+0.015}_{-0.012}$	4.47 $^{+1.79}_{-1.38}$	0.55 $^{+0.05}_{-0.06}$	98.8
	1	4263.57 \pm 0.17	4263.14 \pm 0.18	0.066 $^{+0.022}_{-0.017}$	4.21 $^{+2.32}_{-1.36}$	0.67 $^{+0.06}_{-0.08}$	98.3
	2	4329.12 \pm 2.46	4328.68 \pm 2.46	0.009 $^{+0.002}_{-0.002}$	4.39 $^{+2.43}_{-2.08}$	0.24 $^{+0.08}_{-0.08}$	89.7
28	0	4341.82 \pm 0.91	4341.38 \pm 0.91	0.017 $^{+0.003}_{-0.004}$	4.40 $^{+2.49}_{-2.20}$	0.34 $^{+0.11}_{-0.11}$	98.4
	1	4411.38 \pm 0.27	4410.93 \pm 0.27	0.025 $^{+0.004}_{-0.005}$	4.52 $^{+2.69}_{-2.93}$	0.42 $^{+0.14}_{-0.19}$	44.9

Table 5. Fitted mode parameters of HD 176465 B

n	ℓ	Frequency (μHz)	RV Corr. Freq. (μHz)	Height ($\text{ppm}^2/\mu\text{Hz}$)	Linewidth (μHz)	Amplitude (ppm)	$P(M_{\text{mode}} \mathbf{y})$ %
15	2	2709.26 ± 2.31	2708.98 ± 2.31	$0.033^{+0.011}_{-0.008}$	$0.19^{+0.33}_{-0.10}$	$0.11^{+0.05}_{-0.04}$	59.9
16	0	2725.97 ± 1.56	2725.69 ± 1.56	$0.061^{+0.019}_{-0.016}$	$0.21^{+0.29}_{-0.08}$	$0.16^{+0.06}_{-0.04}$	37.4
	1	2797.21 ± 0.43	2796.92 ± 0.43	$0.092^{+0.029}_{-0.023}$	$0.34^{+0.07}_{-0.15}$	$0.20^{+0.07}_{-0.03}$	40.2
	2	2864.06 ± 1.63	2863.77 ± 1.63	$0.087^{+0.017}_{-0.016}$	$0.38^{+0.15}_{-0.20}$	$0.22^{+0.04}_{-0.07}$	22.6
17	0	2879.67 ± 0.47	2879.38 ± 0.47	$0.164^{+0.032}_{-0.030}$	$0.38^{+0.19}_{-0.21}$	$0.30^{+0.07}_{-0.10}$	41.4
	1	2951.76 ± 0.21	2951.46 ± 0.21	$0.247^{+0.048}_{-0.045}$	$0.58^{+0.11}_{-0.09}$	$0.48^{+0.05}_{-0.06}$	100
	2	3018.83 ± 1.24	3018.52 ± 1.24	$0.078^{+0.013}_{-0.013}$	$0.78^{+0.09}_{-0.11}$	$0.31^{+0.02}_{-0.03}$	15.9
18	0	3032.77 ± 0.42	3032.46 ± 0.42	$0.147^{+0.025}_{-0.025}$	$0.83^{+0.09}_{-0.14}$	$0.43^{+0.04}_{-0.04}$	75.7
	1	3105.54 ± 0.21	3105.23 ± 0.21	$0.220^{+0.037}_{-0.037}$	$1.38^{+0.17}_{-0.16}$	$0.69^{+0.07}_{-0.06}$	100
	2	3173.61 ± 0.71	3173.29 ± 0.71	$0.086^{+0.015}_{-0.013}$	$1.90^{+0.25}_{-0.21}$	$0.51^{+0.03}_{-0.03}$	42.9
19	0	3187.74 ± 0.26	3187.41 ± 0.26	$0.162^{+0.029}_{-0.025}$	$2.01^{+0.27}_{-0.23}$	$0.72^{+0.05}_{-0.04}$	100
	1	3260.58 ± 0.15	3260.25 ± 0.15	$0.243^{+0.043}_{-0.037}$	$1.47^{+0.20}_{-0.14}$	$0.76^{+0.05}_{-0.05}$	100
	2	3328.74 ± 0.44	3328.40 ± 0.44	$0.187^{+0.022}_{-0.022}$	$1.01^{+0.14}_{-0.13}$	$0.55^{+0.03}_{-0.04}$	99.6
20	0	3342.19 ± 0.10	3341.85 ± 0.10	$0.353^{+0.040}_{-0.041}$	$0.91^{+0.15}_{-0.13}$	$0.71^{+0.04}_{-0.07}$	100
	1	3415.97 ± 0.12	3415.62 ± 0.12	$0.530^{+0.060}_{-0.062}$	$1.18^{+0.09}_{-0.15}$	$0.99^{+0.05}_{-0.05}$	100
	2	3485.02 ± 0.62	3484.67 ± 0.62	$0.159^{+0.027}_{-0.018}$	$1.42^{+0.17}_{-0.22}$	$0.60^{+0.02}_{-0.03}$	99.9
21	0	3497.66 ± 0.18	3497.30 ± 0.18	$0.301^{+0.050}_{-0.033}$	$1.46^{+0.19}_{-0.23}$	$0.83^{+0.04}_{-0.04}$	100
	1	3571.11 ± 0.11	3570.75 ± 0.12	$0.451^{+0.074}_{-0.050}$	$1.71^{+0.13}_{-0.21}$	$1.10^{+0.04}_{-0.04}$	100
	2	3641.19 ± 0.36	3640.82 ± 0.36	$0.178^{+0.027}_{-0.018}$	$1.92^{+0.16}_{-0.18}$	$0.73^{+0.04}_{-0.03}$	100
22	0	3652.89 ± 0.17	3652.52 ± 0.17	$0.336^{+0.050}_{-0.033}$	$1.95^{+0.17}_{-0.18}$	$1.01^{+0.05}_{-0.05}$	100
	1	3726.60 ± 0.13	3726.22 ± 0.13	$0.503^{+0.075}_{-0.049}$	$1.83^{+0.22}_{-0.23}$	$1.20^{+0.05}_{-0.05}$	100
	2	3796.59 ± 0.32	3796.20 ± 0.32	$0.113^{+0.017}_{-0.013}$	$1.70^{+0.37}_{-0.31}$	$0.55^{+0.04}_{-0.04}$	100
23	0	3808.17 ± 0.23	3807.79 ± 0.23	$0.212^{+0.032}_{-0.024}$	$1.67^{+0.40}_{-0.32}$	$0.75^{+0.06}_{-0.06}$	100
	1	3882.48 ± 0.26	3882.08 ± 0.26	$0.319^{+0.048}_{-0.035}$	$2.80^{+0.36}_{-0.34}$	$1.19^{+0.05}_{-0.07}$	100
	2	3952.93 ± 0.74	3952.53 ± 0.74	$0.046^{+0.009}_{-0.010}$	$3.84^{+0.64}_{-0.61}$	$0.53^{+0.05}_{-0.08}$	99.7
24	0	3964.72 ± 0.65	3964.32 ± 0.65	$0.087^{+0.017}_{-0.019}$	$4.01^{+0.70}_{-0.66}$	$0.75^{+0.07}_{-0.11}$	100
	1	4038.82 ± 0.53	4038.41 ± 0.53	$0.130^{+0.026}_{-0.028}$	$3.89^{+0.57}_{-0.70}$	$0.88^{+0.11}_{-0.11}$	100
	2	4108.98 ± 1.17	4108.56 ± 1.17	$0.033^{+0.011}_{-0.006}$	$3.72^{+1.15}_{-1.22}$	$0.43^{+0.05}_{-0.04}$	89.3
25	0	4120.30 ± 0.62	4120.87 ± 0.62	$0.063^{+0.021}_{-0.012}$	$3.66^{+1.31}_{-1.29}$	$0.59^{+0.07}_{-0.06}$	100
	1	4195.00 ± 0.52	4194.57 ± 0.52	$0.094^{+0.031}_{-0.017}$	$3.77^{+0.79}_{-0.44}$	$0.75^{+0.10}_{-0.07}$	100
	2	4264.85 ± 2.49	4264.42 ± 2.49	$0.024^{+0.003}_{-0.005}$	$4.09^{+0.72}_{-0.66}$	$0.38^{+0.03}_{-0.03}$	61.3
26	0	4276.86 ± 1.02	4276.42 ± 1.02	$0.045^{+0.006}_{-0.010}$	$4.16^{+0.75}_{-0.85}$	$0.53^{+0.04}_{-0.05}$	85.3
	1	4351.43 ± 0.66	4340.99 ± 0.66	$0.067^{+0.009}_{-0.015}$	$4.44^{+1.53}_{-1.85}$	$0.67^{+0.08}_{-0.13}$	100

Appendix A: “Best Fitter” methodology and priors

The fitting procedure had several steps. First, a global fit over the frequency range $\Delta = [100, 6000] \mu\text{Hz}$ was performed that describes the mode envelopes by two Gaussians (one for each star). The noise background was described by two Harvey-like profiles (Harvey 1985) with the exponent initially fixed at 2, plus a white noise component,

$$N(\nu) = \frac{H_0}{1 + (\tau_0 \nu)^{p_0}} + \frac{H_1}{1 + (\tau_1 \nu)^{p_1}} + N_0. \quad (\text{A.1})$$

Secondly, following the semi-automatic approach from Benomar et al. (2012) we estimated the linewidths⁵ and heights. Input frequencies were obtained by rescaling solar frequencies, as explained in Sect. 4. We then performed a global fit of all individual modes that are significantly above the noise level. For the purposes of efficiency, this was done only over the frequency range $\Delta = [1500, 4600] \mu\text{Hz}$. Note that in this range, the lower-frequency Harvey-like profile does not contribute significantly to the noise background, so it was discarded in further steps.

Priors for all parameters needed to be adequately defined. Two families of priors can be distinguished: (1) generic priors suitable for most solar-like oscillators and (2) priors set after visual inspection of the power spectrum. For convenience we first recall the definition of the indicator function for $x \in \mathbb{R}$, the extend real line, and $a, b \in \mathbb{R}$ and such that $a < b$,

$$\mathbb{1}_{[a,b]}(x) = \begin{cases} 1 & \text{if } x \in [a, b] \\ 0 & \text{otherwise.} \end{cases} \quad (\text{A.2})$$

Appendix A.1: Generic priors

Generic priors are those which are not specifically tuned for the HD 176465 binary system, but are suitable for most cool main-sequence solar-like oscillators. Table A.1 summarizes the nature of the priors. In this category, two kinds of priors were used: the Jeffrey-truncated prior and the uniform prior (Jeffreys 1961). The Jeffrey-truncated⁶ prior,

$$J(x; a, b) = \frac{\ln(1 + b/a)}{x + a} \mathbb{1}_{[a,b]}(x), \quad (\text{A.3})$$

can be appropriate in the case of a scale parameter (i.e. a parameter such as $f(x) = ax$ with a , a scale factor), which is the case for the heights and widths of the modes. Note that this prior is non-informative and uniform in the logarithmic domain so that it is invariant under parameter transformation in a logarithmic scale.

The uniform prior defined as,

$$U(x; a, b) = \frac{1}{b - a} \mathbb{1}_{[a,b]}(x), \quad (\text{A.4})$$

is recommended by Jeffreys for location parameters (i.e. parameters such as $f(x) = x + a$), which is the case, for example, for the mode frequencies or the rotational splitting.

⁵ Mode widths are estimated using Fig. 4b from White et al. (2012), which shows the empirical relation between the width and the asymptotic frequency phase, ϵ .

⁶ Note that this prior is truncated because its integral would be otherwise undefined.

Table A.1. Generic priors and noise priors used during the fit of the mode parameters of the HD 176465 binary system.

Parameter type	Prior	Unit
Mode height H	$J(1, 250)$	$\text{ppm}^2/\mu\text{Hz}$
Mode width Γ	$J(0.5, 40)$	μHz
Mean rotational splitting ν_s	$U(0, 3.5)$	μHz
Stellar inclination i	$U(0, 90)$	degree
Noise height H_1	$G(0.417, 0.036)$	$\text{ppm}^2/\mu\text{Hz}$
Noise timescale τ_1	$G(999, 214)$	second
Noise power p_1	$G(2.0, 0.1)$	no unit
White noise N_0	$G(0.2307, 0.0045)$	$\text{ppm}^2/\mu\text{Hz}$

Appendix A.2: Priors specific to the HD 176465 system

The parameters of the noise background and oscillation frequencies require specific priors for HD 176465 A and B.

Regarding the noise background, we used Gaussian priors defined as $G(x; x_c, \sigma) = e^{-0.5(x-x_c)^2/\sigma^2} / \sqrt{2\pi}\sigma$ for all of the parameters of the noise function, H_1 , τ_1 , p_1 and N_0 . The characteristic values for x_c and σ are given in Table A.1.

The priors for the oscillation frequencies must limit the range of acceptable values in order to achieve the correct mode identification. This is especially critical in the case of HD 176465, as the two components of the binary system oscillate at similar frequencies so that individual modes of the stars may overlap.

One could use uniform priors to define the acceptable range for a given pulsation frequency. However, a trial and error approach over large set of solar-like oscillators showed that choosing uniform priors with Gaussian edges for frequencies defined as,

$$F(x; a, b, \sigma) = C \exp\left[-\frac{1}{2} \frac{(x-a)^2}{\sigma^2}\right] \mathbb{1}_{]-\infty, a[}(x) + C \mathbb{1}_{[a, b]}(x) + C \exp\left[-\frac{1}{2} \frac{(x-b)^2}{\sigma^2}\right] \mathbb{1}_{[b, +\infty[}(x) \quad (\text{A.5})$$

enhanced the stability during the training phase of the MCMC process when dealing with a large parameter space (see Benomar et al. 2009b, for more details about the training phase). Here, $C = (b - a + 0.5 \sqrt{2\pi}\sigma)^{-1}$ is the normalization constant and $\sigma = 0.2 \mu\text{Hz}$. Values of the boundaries a and b for each mode are given in table A.2 for HD 176465 A and A.3 for HD 176465 B.

The fit of HD 176465 was complicated by the overlapping frequencies of the stars. This is evident from the échelle diagrams in Fig. 3. When this occurs, it is not possible to unambiguously separate the power due to one star from the other unless further priors are defined. As described by Equation (1), p modes of each star are approximately regularly spaced, so that the second derivative in radial order n of that equation is $\frac{\partial^2 \nu(l, n)}{\partial n^2} \approx 0$. Thus one may limit local strong deviations from the regular pattern by imposing a Gaussian prior so that $\frac{\partial^2 \nu(l, n)}{\partial n^2} = G(0, \sigma)$. Numerically, the second derivative was performed using a forward/backward difference on the edges and an entered difference otherwise. A value of $\sigma = 2 \mu\text{Hz}/n^2$ was found to be suitable to de-correlate the overlapping modes.

Appendix A.3: Mode significance

The mode significance was determined by locally fitting each mode of frequency $\nu(n, l)$ over $\Delta = [\nu(n, l) - \Delta\nu/3, \nu(n, l) + \Delta\nu/3]$,

Table A.2. Frequency priors for HD 176465 A, along with the fitted frequency. The prior is uniform in the range $[x_{\min}, x_{\max}]$ but has Gaussian edges with standard deviation $\sigma = 0.2 \mu\text{Hz}$.

n	ℓ	Output Frequency (μHz)	$[a, b]$
12	2	2121.39 \pm 1.67	[2116.99, 2134.32]
13	0	2132.67 \pm 0.61	[2127.84, 2135.17]
	1	2202.44 \pm 0.39	[2197.82, 2204.35]
	2	2268.74 \pm 1.17	[2262.39, 2281.03]
14	0	2280.58 \pm 0.90	[2269.85, 2285.97]
	1	2348.98 \pm 0.24	[2339.54, 2358.89]
	2	2415.63 \pm 1.97	[2410.13, 2430.27]
15	0	2428.06 \pm 0.38	[2423.23, 2440.56]
	1	2496.73 \pm 0.33	[2491.47, 2503.45]
	2	2561.06 \pm 1.65	[2555.72, 2577.18]
16	0	2575.83 \pm 0.83	[2565.60, 2587.66]
	1	2642.66 \pm 0.10	[2640.57, 2646.71]
	2	2706.15 \pm 0.74	[2698.51, 2717.15]
17	0	2720.12 \pm 0.28	[2713.56, 2723.17]
	1	2788.08 \pm 0.36	[2783.74, 2793.14]
	2	2852.75 \pm 0.38	[2846.03, 2858.21]
18	0	2865.49 \pm 0.09	[2863.66, 2867.32]
	1	2934.23 \pm 0.12	[2931.46, 2937.10]
	2	2999.34 \pm 0.22	[2991.83, 3005.24]
19	0	3012.10 \pm 0.11	[3006.55, 3014.44]
	1	3081.19 \pm 0.10	[3077.39, 3086.70]
	2	3146.38 \pm 0.21	[3139.26, 3153.16]
20	0	3158.74 \pm 0.02	[3154.07, 3162.85]
	1	3227.97 \pm 0.09	[3224.83, 3230.38]
	2	3293.79 \pm 0.17	[3289.20, 3299.27]
21	0	3305.62 \pm 0.08	[3301.69, 3310.76]
	1	3375.32 \pm 0.10	[3369.81, 3380.09]
	2	3441.16 \pm 0.36	[3433.29, 3448.81]
22	0	3452.35 \pm 0.11	[3447.70, 3457.17]
	1	3522.07 \pm 0.14	[3514.91, 3528.31]
	2	3588.47 \pm 0.26	[3583.73, 3593.71]
23	0	3599.69 \pm 0.13	[3593.41, 3605.80]
	1	3669.46 \pm 0.16	[3664.65, 3675.13]
	2	3735.42 \pm 0.63	[3731.54, 3743.92]
24	0	3746.85 \pm 0.16	[3742.64, 3752.11]
	1	3817.25 \pm 0.24	[3812.14, 3822.83]
	2	3884.21 \pm 1.72	[3876.05, 3892.18]
25	0	3895.17 \pm 0.18	[3890.94, 3900.05]
	1	3965.06 \pm 0.40	[3959.44, 3971.12]
	2	4033.13 \pm 1.44	[4022.67, 4045.10]
26	0	4043.26 \pm 0.02	[4032.42, 4048.46]
	1	4114.50 \pm 0.50	[4109.93, 4121.31]
	2	4181.86 \pm 0.89	[4173.92, 4190.65]
27	0	4192.29 \pm 0.46	[4187.77, 4202.42]
	1	4263.57 \pm 0.17	[4252.20, 4273.98]
	2	4329.12 \pm 2.46	[4322.77, 4343.90]
28	0	4341.82 \pm 0.91	[4334.49, 4344.79]
	1	4411.38 \pm 0.27	[4394.87, 4417.14]

Table A.3. Frequency priors for HD 176465 B, along with the fitted frequency. The prior is uniform in the range $[x_{\min}, x_{\max}]$ but has Gaussian edges with standard deviation $\sigma = 0.2 \mu\text{Hz}$.

n	ℓ	Output Frequency (μHz)	$[a, b]$
15	2	2709.26 \pm 2.31	[2706.26, 2712.74]
16	0	2725.97 \pm 1.56	[2721.93, 2729.03]
	1	2797.21 \pm 0.43	[2793.96, 2799.60]
	2	2864.06 \pm 1.63	[2858.83, 2874.60]
17	0	2879.67 \pm 0.47	[2874.39, 2882.85]
	1	2951.76 \pm 0.21	[2947.15, 2955.30]
	2	3018.83 \pm 1.24	[3014.32, 3027.06]
18	0	3032.77 \pm 0.42	[3027.58, 3037.39]
	1	3105.54 \pm 0.21	[3099.83, 3113.54]
	2	3173.61 \pm 0.71	[3166.46, 3181.40]
19	0	3187.74 \pm 0.26	[3182.02, 3192.57]
	1	3260.58 \pm 0.15	[3255.83, 3263.87]
	2	3328.74 \pm 0.44	[3325.40, 3337.20]
20	0	3342.19 \pm 0.10	[3338.90, 3349.95]
	1	3415.97 \pm 0.12	[3408.26, 3422.71]
	2	3485.02 \pm 0.62	[3479.63, 3494.25]
21	0	3497.66 \pm 0.18	[3494.04, 3500.83]
	1	3571.11 \pm 0.11	[3567.12, 3575.47]
	2	3641.19 \pm 0.36	[3634.79, 3648.60]
22	0	3652.89 \pm 0.17	[3648.49, 3656.32]
	1	3726.60 \pm 0.13	[3722.61, 3731.03]
	2	3796.59 \pm 0.32	[3789.15, 3803.87]
23	0	3808.17 \pm 0.23	[3804.39, 3811.49]
	1	3882.48 \pm 0.26	[3877.57, 3886.14]
	2	3952.93 \pm 0.74	[3947.14, 3959.36]
24	0	3964.72 \pm 0.65	[3959.25, 3970.32]
	1	4038.82 \pm 0.53	[4034.73, 4044.13]
	2	4108.98 \pm 1.17	[4105.34, 4118.61]
25	0	4120.30 \pm 0.62	[4116.52, 4128.74]
	1	4195.00 \pm 0.52	[4192.20, 4199.83]
	2	4264.85 \pm 2.49	[4262.82, 4273.99]
26	0	4276.86 \pm 1.02	[4270.65, 4282.76]
	1	4351.43 \pm 0.66	[4347.48, 4356.78]

where $\Delta\nu$ is the large separation. Two fits were required to make a model comparison possible. The first fit uses a model M_{mode} that included the mode for which the probability was calculated, along with a noise model. The second fit included only the noise model M_{noise} . Using Equation (4), the Bayes factor was calculated assuming the *a priori* equiprobability of the two models, $\pi(M_{\text{noise}}) = \pi(M_{\text{mode}}) = 0.5$, so that

$$P(M_{\text{mode}}|y) = \frac{1}{1 + \pi(y|\text{noise})/\pi(y|\text{mode})}. \quad (\text{A.6})$$

More details about the technical implementation to calculate $\pi(y|\text{noise})$ and $\pi(y|\text{mode})$ can be found in Benomar et al. (2009a). Note that within Δ , modes other than the one for which we wished to calculate the probability could be present. These were included as a part of the noise background, with parameters fixed to their median values obtained during the global fit. Note also that the two fits were made with the same priors as for the global fit.